

Ab Initio Molecular Dynamics Study of Nanoscale Heat Transfer and Energy Conversion

A Thesis

Presented to the

Faculty of the Graduate School

University of Missouri-Columbia

In Partial Fulfillment

of the Requirement for the Degree of

Master of Science

By

Pengfei Ji

Dr. Yuwen Zhang, Thesis Supervisor

May 2013

The undersigned have examined the thesis entitled

**Ab Initio Molecular Dynamics Study of
Nanoscale Heat Transfer and Energy Conversion**

Presented by Pengfei Ji

A candidate for the degree of Master of Science in Mechanical & Aerospace Engineering
and hereby certify that in their opinion it is worthy of acceptance

Dr. Yuwen Zhang

Dr. Robert Tzou

Dr. Carol A. Deakne

ACKNOWLEDGEMENTS

At the special moment of accomplishing the dissertation, I would like thank my advisor Dr. Yuwen Zhang for providing me patient guidance, warm-hearted encouragement, and long term support. I am highly grateful for his help since I enrolled in MU, both academic research and daily life.

I would like to thank all the member of my thesis evaluation committee, Dr. Tzou and Dr. Deakyne for taking the time to provide valuable comments and criticism.

I would like to express my particular thanks to Dr. Rober Tzou, Chairman of Department of Mechanical and Aerospace Engineering for enlightening my dream of academic career and offering me greatly precious opportunity to study in MU. Thank Dr. Tzou to instruct to me bridge the engineering application with the theoretically and fundamentally academic research. Inspired by his broadness and depth of knowledge, and passion to explore the unknown field of great potential in nanoscale heat transfer problems, I carried out this exciting project.

Thank Dr. Deakyne to bring me to get a further sight into the electronic structure calculation and density functional theory.

Support for this work by the U.S. National Science Foundation under Grant Number CEBT-1066917 is gratefully acknowledged. I also thank the University of Missouri Bioinformatics Consortium (UMBC) for providing supercomputing resource.

I would like to thank all my coworkers, Yijin Mao, Zheng Li, Nazia Afrin, Hamid, Xin Dou. It is a really wonderful time to work with all of them.

Special thanks are to my parents, who stand by me and give me the courage and strength to support me carry on my research every time when I encountered difficulties. Without all the love and support I have received all these years from my parents, I would never have been able to successfully reach my academic goals.

TABLE OF CONTENTS

ACKNOWLEDGEMENTS	ii
LIST OF FIGURES	vi
LIST OF TABLES	ix
ABSTRACT	x
NOMENCLATURE	xiii
Chapter 1 Introduction.....	1
Chapter 2 Theory of Ab Initio Molecular Dynamics	12
2.1 Born-Oppenheimer Approximation	12
2.2 Density Functional Theory.....	15
2.3 Car-Parrinello Molecular Dynamics	17
2.4 Ab Initio Molecular Dynamics with Excited Electrons	22
Chapter 3 Car-Parrinello MD Study of Structural, Dynamic, and Vibrational Properties of Si/Ge Superlattices during Heat Transfer.....	26
3.1 Modeling and Simulation.....	26
3.2 Results and Discussion.....	29
3.2.1 Temperature Evolutions with Simulation Time Steps	29
3.2.2 Translation Dynamics at Different Simulation Stages.....	31
3.2.3 Vibrational Density of States Analyses	34

Chapter 4	Car-Parrinello MD Simulation of Atomic Scale Energy Transport: From Heat Conduction to Thermal Radiation	37
4.1	Modeling and Simulation Details.....	37
4.2	Results and Discussion.....	39
4.2.1	Pure Material Combinations	39
4.2.2	Hybrid Materials Combinations.....	45
Chapter 5	Femtosecond Laser Processing of Germanium: An Ab Initio Molecular Dynamics Study	56
5.1	Modeling and Simulation.....	56
5.2	Results and Discussion.....	60
5.2.1	Temperature Evolutions.....	60
5.2.2	The Free Energy Calculation	62
5.2.3	Nanostructure Changes due to Thermal Melting and Evaporation.....	65
5.2.4	Thermal Motion of Atoms	69
5.2.5	Dynamical Property of Velocity Autocorrelation Function.....	73
5.2.6	Vibrational Density of States Analysis.....	75
Chapter 6	Summary and Conclusion.....	77
	REFERENCES	81

LIST OF FIGURES

Fig. 1 Supercell for the Si/Ge superlattices modeling	26
Fig. 2 Periodically alternating Si/Ge superlattices.....	28
Fig. 3 Temperature evolution curves obtained from MD simulation	30
Fig. 4 MSDs in different simulation stages	33
Fig. 5 Vibration spectra of the simulated Si/Ge superlattices.....	35
Fig. 7 Simulation box of silicon-germanium-layer combination with the Interfacial distance equals the lattice constant of germanium.....	38
Fig. 7 Silicon-silicon-layer combination: (a) attached to each other, (b) interfacial distance: 1.0 lattice constant of silicon, (c) interfacial distance: 2.0 lattice constant of silicon.....	41
Fig. 8 Germanium-germanium-layer combination: (a) attached to each other, (b) interfacial distance: 1.0 lattice constant of germanium, (c) interfacial distance: 2.0 lattice constant of germanium.....	44
Fig. 9 Silicon-germanium-layer combination (400 K vs. 100 K) : (a) attached to each other, (b) interfacial distance: 1.0 lattice constant of germanium, (c) interfacial distance: 2.0 lattice constant of germanium.....	47

Fig. 10 Silicon-germanium-layer combination (100 K vs. 400 K) : (a) attached to each other, (b) interfacial distance: 1.0 lattice constant of germanium, (c) interfacial distance: 2.0 lattice constant of germanium.....	48
Fig. 11 Periodic display of the silicon-germanium-layer combination in y- and z- direction (the interfacial distance equals the lattice constant of germanium).....	52
Fig. 12 Schematic show of the incident waves, emitted waves, evanescent waves during the electromagnetic waves emission process	54
Fig. 13 Ionic temperatures	60
Fig. 14 Free energies for all the cases.....	62
Fig. 15 Free energy change for different cases	64
Fig. 16 RDF of germanium crystal at room temperature (300 K).....	66
Fig. 17 RDFs at different stages, solid state (20,000 K).....	67
Fig. 18 RDFs at different stages, liquid state (30,000 K).....	68
Fig. 19 RDFs at different stages, gas phase (60,000 K).....	68
Fig. 20 MSD of germanium crystal at room temperature (300 K).....	69
Fig. 21 MSDs at different stages, solid state (20,000 K)	71
Fig. 22 MSDs at different stages, liquid state (30,000 K).....	72
Fig. 23 MSDs at different stages, gas state (60,000 K).....	72

Fig. 24 VAFs of cases calculated from 1,000 time steps simulation..... 73

Fig. 25 VDOS of cases sample from 1,000 time steps simulation 76

LIST OF TABLES

Table 1	Equilibration time for silicon-silicon-layer combinations under different interfacial distance	40
Table 2	Equilibration time for germanium-germanium-layer combinations under different interfacial distance	43
Table 3	Equilibration time for silicon (400 K) - germanium (100 K) - layer combinations under different interfacial distance.....	50
Table 4	Equilibration time for silicon (100 K) - germanium (400 K) - layer combinations under different interfacial distance.....	50
Table 5	Femtosecond Laser Parameters in the Simulation.....	59

ABSTRACT

In this thesis, ab initio molecular dynamics simulation based on a plane wave/pseudopotential implementation of density functional theory was adopted to investigate nanoscale heat transfer and energy conversions for semiconductors.

The first one investigates the heat conduction process occurring in Si/Ge superlattices at selected stages from the initial point of nonzero temperature gradient to the final state of thermal equilibrium. The ab initio molecular dynamics simulation was performed to get deep sight into the detailed information of the structural, dynamic and vibrational properties of Si/Ge superlattices. The statistical comparisons of temperature evolution curves were made according to the kinetic theory. The ab initio molecular dynamics simulation outputs in the work shows reasonable thermophysical results of the thermal energy transport process. The radial distribution functions and mean square displacements were calculated and further discussions were made to explain and probe the structural changes relating to the heat transfer phenomenon. Furthermore, the vibrational density of states of the two layers (Si/Ge) were computed and plotted to analyze the contributions of phonons with different frequencies to the heat conduction. Coherent heat conduction of the low frequency phonons was found and their contributions to facilitate heat transfer were confirmed.

The second one studies the thermal energy transportation phenomena spanning from heat conduction of thermal radiation with the modeling of variable gap distances in different thin layer systems. By imposing thermostats to keep constant temperatures of the

nanoscale thin layers, the initial thermal non-equilibrium between the neighboring layers was established under the vacuum condition. The ab initio simulations were carried out for different material combinations and interfacial distances of silicon and germanium layers. The results show significant distinctions of heat transfer under different materials and temperatures combinations. Further discussions on the equilibrium time were made to explain the simulation results.

The third one presents an ab initio molecular dynamics study of femtosecond laser processing of germanium is presented in this paper. The method based on the finite temperature density functional theory is adopted to probe the nanostructure change, thermal motion of the atoms, dynamic property of the velocity autocorrelation, and the vibrational density of states. Starting from a cubic system at room temperature (300 K) containing 64 germanium atoms with an ordered arrangement of 1.132 nm in each dimension, the femtosecond laser processing is simulated by imposing the Nose Hoover thermostat to the electronic subsystem lasting for ~ 100 fs and continuing with microcanonical ensemble simulation of ~ 200 fs. The simulation results show solid, liquid and gas phases of germanium under adjusted intensities of the femtosecond laser irradiation. We find the irradiated germanium distinguishes from the usual germanium crystal by analyzing their melting and dynamic properties.

As the first work of studying the nanoscale energy transport spanning from heat conduction to thermal radiation and the femtosecond laser material interaction in mechanical engineering, the simulation results highlight the promising application of the first-principles molecular dynamics in thermal engineering. We believe our results and the conclusion drawn will be quite useful in helping to resolving the heat transfer and

energy conversion problem during the miniaturization of integrated circuits and molecular electronics.

NOMENCLATURE

<i>a</i>	lattice vector, Bohr = 0.52917720859 Å
<i>b</i>	reciprocal lattice vector, Bohr ⁻¹
<i>c</i> ₀	speed of light in vacuum, m/s
<i>c</i>	conversion coefficient, eV/K
<i>d</i>	length of the simulation system in one direction, Å
<i>E</i>	atomic-scale energy, J
<i>f</i> _{<i>i</i>}	Fermi-Dirac occupation number
<i>f</i> _{<i>G</i>} ^{PW}	plane wave basis
<i>g</i>	a vector with triple of integer values, Bohr
<i>G</i>	reciprocal space vector, Bohr ⁻¹
<i>h</i>	lattice matrix
<i>J</i>	femtosecond laser fluence, J/cm ²
<i>k</i>	wave vector
<i>k</i> _B	Boltzmann constant, 1.38 × 10 ⁻²³ J/K
<i>M</i>	atomic mass, a. u. = 0.00054857990943 a. m. u
<i>n</i>	index of refraction

\mathbf{R}	atomic position vector, Bohr
\mathbf{R}^N	union of all the atomic position vectors
\mathbf{r}	position vector
s	coordinates scalar
T_S	kinetic energy of a non-interacting system, Ha
U	potential, Ha
v	velocity, Bohr/a. t. u
\mathbf{V}_i	three components of the velocity $v_x(t)$, $v_y(t)$ and $v_z(t)$
V_{ext}	external potential, Ha
V_H	Hartree potential, Ha

Greek

β	electronic temperature parameter
ε^{KS}	extended Kohn-Sham energy function, Ha
δ_{ij}	orthonormality relation, $\langle \phi_i \phi_j \rangle$
μ_i	fictitious mass, a. u.
μ	chemical potential, Ha
Ω	volume of the unit cell, a. u. ³
θ	angle of the electromagnetic wave, °

ω	frequency of the incident energy, Hz
ρ	electronic density
\mathcal{L}	Lagrangian form of energy, Ha
ϕ	Hartree potential, Ha
ψ_i	one-electron eigenstates
\mathcal{F}	Helmholtz free energy, Ha
\mathcal{H}	Hamiltonian form of energy, Ha
Ψ	electronic wave function
Ω	ground potential for an interacting spin Fermi gas, Ha
ϕ	electronic orbital
λ	wave length, m
ν	vibrational frequency of atom, s^{-1}

Superscripts

PW	plane wave
KS	Kohn-Sham
occ	occupied orbitals
N	union of all the positions

Subscripts

c critical point of total internal reflection

i incidence of wave

e electron

i incidence of wave

I ion

NINT nearest integer value

pb periodic boundary condition

tw thermal wave

vol volume of the modeled system

xc exchange correlation in DFT

Chapter 1 Introduction

As the integrated circuits (ICs) are being miniaturized, complementary metal-oxide-semiconductor (CMOS) has stepped into the fabrication era of 22-nm for the central processing unit (CPU) since 2011 by Intel [1]. Transistor size and structure plays a crucial role in fulfilling the Moore's Law [2]. With the continuing improvement of manufacturing technology, the execution efficiency is also being improved. The 22-nm processors, which are known as 3-D Tri-Gate transistor using three gates wrapped around the silicon channel in a 3-D structure, bring unprecedented computational performance, and accompany tremendous heat generation. Hence, the nanoscale heat transfer and thermoelectric transport should be considered during the miniaturization process. Understanding the atomic-scale thermal characterization and the control of materials species, interfaces, and structures are of the prime importance.

In addition, the International Technology Roadmap for semiconductors (ITRS) 2006 Front End Process Update indicates that equivalent physical oxide thickness will not scale below 0.5 nm, which is approximate twice the diameter of a silicon atom. Through the X-ray diffraction experiment, superlattices (SLs) were discovered in the early 20th century according to their special patterns. For semiconductor SLs, the idea was originated by Esaki and Tsu [3]. As envisioned, there are two kinds of SLs: one is compositional and the other is doping. The compositional SLs are consisted of alternating super thin layers of two more other kinds of materials that have nearly the same lattice parameters. In general, the thicknesses of individual layer are in the range between

angstroms to nanometers. In the compositional SLs, the electronic potential is modulated on a length scale that is shorter than the electron mean free path by the layer composition. As for the doping SLs, they cover alternating n- and p-type layers of a single semiconductor. The electric fields generated by the charged dopants play the role of modulating the electronic potential. The cutting-edge nanotechnology has been the driving force to lead the development of novel applications and devices based on the SLs. One of the most important parts of the design of SLs is the thermal management. The microsystem will fail or even break due to overheat, if the thermal energy generated inside the SLs cannot be transported away efficiently. Understanding the heat transfer process occurring in the semiconductor SLs has been an issue of great importance in the composited semiconductors fabrication. Consequently, to probe thermal transport will produce far reaching influence to the future development of thermal management of ICs. The interfacial thermal resistance plays a critical role in the heat conduction process between the neighboring layers. In this work, heat transfer process for the SLs composed of silicon and germanium layers with periodicity will be investigated.

In the manufacturing process, it is inevitable to leave gaps/defects inside the transistor packages at the length of the atomic-scale. Thermal radiation coexists with thermal conductance that occurs at such confined geometrical structures. Due to the ubiquitous gaps in synthetic materials, especially in the fabricated ICs, understanding and predicting the heat transfer between two bodies separated by a distance of atomic-scale have been a key issue in both theoretical and application points of view [4]. In addition, with the reduction of the size of structure, the thermodynamics properties of nanoscale thin films significantly differ from that of the bulk materials [5]. As demonstrated, the thermal

conductivity of silicon renders a tendency of decrease when the thickness of a layer is less than 1000 \AA [6]. Thermal energy transport is no longer a pure conceptual phenomenon but has become a crucial topic in the field of thermal management of micro-electro-mechanical systems (MEMS) and nano-electro-mechanical systems (NEMS) [7].

During the past two decades, in the fields of fabrication of microelectronic and optoelectronic devices, thermal electronic and thermionic devices [8], the heat transfer phenomenon in SLs is increasingly recognized and drawn considerable attentions [9]. When it comes to investigate the energy transport efficiency, usually, it refers two opposite goals, namely, to enhance or decrease the heat transfer inside the SLs materials. For the case of microelectronics devices, which are composited with layers of different conductive materials, the object is to increase the thermal conductance between the neighboring layers in order to move the heat generated by Joule effect and realize the purpose of efficient cooling. On the contrary, as for the thermoelectric materials, to lower the overall thermal transport efficiency by mixing dissimilar crystalline materials and artificially adding grain boundaries and gaps is the primarily goal.

Because of the existence of temperature gradient in the materials, the difference of vibrational energies between adjacent atoms causes them to collide with each other. It leads to diffusive transfer of kinetic energy through particles inside the materials. Heat transfer occurs spontaneously from materials at higher temperatures to those at lower temperatures. Energy carriers, such as phonons [10] and free electrons [11], play crucial rules in solid state heat conduction. From the nanoscopic point of view, the thermal energy is transported by different energy carriers like phonons, electrons, or molecules. For semiconductor SLs, phonons are the major energy carriers that move through the

stack of thin layers. In a material with many layers, such scattering effects would accumulate so that the thermophysical properties of semiconductor SLs are strongly impacted by phonon motion inside the layers and scattering at the layer interfaces. It has been a high demand to understand the atomic level mechanism during the heat transfer process in SLs. The microstructure changes of the SLs induced by the heat flow penetrating through the alternating layers will also affect the thermal transporting efficiency. As described in experimental studies on Si/Ge SLs [12], the nanostructure based on samples grown by metal-organic chemical vapor deposition on GaAs substrates with Ge buffers, showed reduced thermal conductivity compared with the bulk materials. In order to come up with appropriate explanations for the experimental findings, researchers proposed various models for the solution of heat conduction in SLs, e.g., the Boltzmann transport equation [13], the phonon group velocity reduction due to zone folding [14,15], and the atomistic Green's function methods [16,17]. Moreover, some of the publications even suggested the potential application of control the conduction of heat by mass-loading nanotubes with heavy molecules [18], manipulating the band formation [19] and creating phonon-surface roughness heat transfer condition [20].

As for the thermal radiation, heat transfer is realized by electromagnetic radiation generated by the motion of charged particles in the matter. The spectrum emissive power of blackbody radiation is a well-understood physical phenomenon that depends on the object's temperature and obeys Plank's law. The Stefan-Boltzmann's law can be used to obtain emissive power of blackbody surface. However, it is only true for objects' distances that are sufficiently large compared with the thermal wave length λ_{tw} given by Wien's law. The typical wavelengths involved in thermal radiation are in the order of

microns [21]. For the heat transfer with an interfacial distance of angstroms to nanometers, the radiation mechanism may change dramatically [22]. When two bodies are separated by a distance that is comparable or much shorter than the dominant emission wavelength, the validity of the classical radiative transfer equations is challenged, as the wave nature of thermal radiation needs to be taken into account.

Electronic charge and thermal energy transport in nanometer scale and ultra-short time scale (from femtoseconds to nanoseconds) have drawn attentions from scholars and have been studied extensively in the past decades. For heat conduction, a unified constitutive equation covering the transport behaviors of diffusion, phonon electron interaction and pure phonon scattering was proposed by Tzou in 1995 [23]. For thermal radiation, a bimaterial atomic force microscope cantilever was used by Narayanaswamy et al. [24] to obtain the “heat transfer-distance” curves between a sphere and a substrate. Their results showed that the enhancement of heat transfer exceeded that predicted by Planck’s blackbody radiation theory. The surface phonon polariton was the factor that caused thermal fluctuations of the electromagnetic field. Two parallel glass surfaces were employed by Hu et al. [25] to measure the radiative heat flux across the micro gaps. Volokitin and Persson [26] studied heat transfer between the two parallel semi-infinite bodies separated by sub-wavelength distance via electromagnetic interaction. As it was reported in the literature, with the interfacial distance decreasing, the heat transfer increased dramatically. But the physical mechanism behind such increase still remains to be undiscovered. Kittel et al. [27] reported a measurement to obtain the heat transfer rate with the distance between microscope tip and sample. However, the measured results differed distinctly from the divergent behavior predicted by standard macroscopic

fluctuating electrodynamics. They interpreted the results in terms of finite microscopic correlations inside the materials.

Femtosecond laser processing has been widely used in the fabrication process of cutting-edge semiconductor integrated circuits (ICs) and nanoelectromechanical systems (NEMS). The photolithography, serving as a conventional approach to fabricate the microstructures, has been a predominant technique since the emergent of semiconductors. However, the traditional photolithography suffers from the drawbacks of high cost and complex treatment for the masks with the miniaturization of structure due to optical diffraction in nanoscale. The femtosecond laser processing (nanolithography), due to its inherent advantages of maskless super resolution [28], offers a potential solution for the high mask cost. In addition, compared with the nanosecond pulses, the femtosecond laser has the advantages of high peak power intensity and a relatively smaller heat-affected zone, which make it ideal for a wide range of applications in other fields of material sciences [29–33]. In many engineering applications ranging from laser micromachining to surface treatment, the femtosecond laser material interaction has become an increasingly hot topic. The laser intensity of femtosecond laser can even be up to 10^{21} W/m^2 [34], which results in the breaking down of traditional phenomenological laws. Hence, for the purpose of achieving a better comprehension and understanding of the femtosecond laser nanolithography, it is of great necessity to investigate the melting and dynamic effects relating with energy transfer and conversion in the atomic scale.

The laser material interaction has attracted considerable attentions in the past two decades due to both the relevant technological importance and theoretical interest. Because the characteristic times of the energy carriers are comparable to the characteristic energy

excitation time, there are two competing interpretations to the thermal mechanical phenomena: one is the plasma annealing, another one is thermal annealing. The plasma annealing describes the microscopic mechanism as the lattices of semiconductors directly transform into a disordered state long before the system become thermally excited. For semiconductors, like silicon, phonons are the major energy carriers. Because the free electron density in semiconductor is much lower than that in metal, the participation of electrons can be neglected. The mechanism under femtosecond laser irradiation is generally regarded as an athermal transition, which mainly softens the interatomic bonds in the time domain that is long before the conventional thermal transition caused by heat transfer from the electrons to phonons [35]. After femtosecond laser irradiation, the electrons transform from the bonding to antibonding states by depleting the bond charges. In other words, when the stage of disordering of the latter happens, the ion temperature still remains at room temperature. The other alternative explanation is the thermal melting [36], which requires the direct energy transfer between the excited electrons and the ions. Due to the electron-phonon coupling, the large amount of excited electron energy transfers to ions within the picoseconds time domain, which causes thermal melting of the lattice.

For the femtosecond laser, the pulse duration is shorter than the electron-lattice thermalization time (in the order of picosecond). Because the excited electrons do not have sufficient time to transfer a large amount of energy to the ions, plasma annealing seems to be the dominating mechanism. The ultrashort laser pulse makes it possible to excite the electronic states of a solid long before the appreciable energy transporting to the lattice vibrational states. Shank *et al.* [37] showed transition from crystalline order to

disorder with melting of the surface occurred in less than 1 *ps* under 90 *fs* laser illumination on silicon. Rousse *et al.* [38] reported the nonthermal melting process in InSb at femtosecond resolution by using a ultrafast time resolved X-ray diffraction. An atomic-scale visualization of internal dynamics presented by Lindenberg *et al.* [39] demonstrated the athermal transition from crystalline solid to disordered liquid.

Besides the above theoretical modeling and analysis, molecular dynamics (MD) simulation paves a new way to investigate the thermal energy transport phenomenon in SLs. Comparing with experimental investigation, theoretical reasoning and numerical simulation can obtain results under extreme conditions that experiments cannot achieve. Since the MD method was firstly introduced by Alder and Wainwright in the 1950s [40,41], MD has been widely applied to study the structural, dynamical, and thermophysical properties of complex systems. The MD simulation results can be used to determine macroscopic thermodynamic properties of the system based on ergodic hypothesis [42], in which the statistical ensemble averages are assumed to be equal to time averages of the system. It has been termed “statistical mechanics by numbers” of predicting the future by animating the natural forces and enable us sight into the thermal energy transport in atomic scale. In terms of classical MD [43], the interatomic force and acceleration used for generating trajectories are based on the first order and second order derivatives of predefined empirical potential functions. The classical MD calculation of thermal interface conductance was carried out by Chalopin *et al.* [44] using equilibrium MD with variable thickness, and showed the evanescent modes when the layer thickness is below 5 *nm*. For nonequilibrium MD simulations, a lattice thermal conductivity for GaAs/AlAs was calculated by Imamura *et al.* [45] with hot and cold reservoirs to produce

heat flow running from one end to the other. For the cases of rough interfaces, Termentzidis *et al.* [46] obtained the in-plane thermal conductivities in binary Lennard-Jones SLs by setting up different characteristic heights of roughness.

However, due to the dependence of predefined potential function to the forces acting on atoms and molecules, the accuracy and application are restricted by the available potential functions. In addition, to tackle the problems, we are facing on thermal transport issues in atomic-scale via a comprehensive simulation of the thermal radiation involving electromagnetic fluctuation, for the shortcoming that classical MD fails to take dynamical electrons impact into account. The implementation of simulation [47] offers us an effective alternative. As one of the *ab initio* MD approaches, CPMD simulation is aimed to perform a simulation in which the interatomic forces are derived directly from the electronic ground state using the Hellman-Feynman theorem. In CPMD, for a given atomic configuration, the Born-Oppenheimer (BO) [48] potential energy surface is obtained by minimizing the total energy functional with respect to one electron states. The CPMD theory will be explained in Chapter 2 in detail.

The *ab initio* MD based simulations of atomic-scale interfacial thermal transport have not been widely investigated and documented. Luo and Lloyd [49] pioneered the first-principles non-equilibrium MD simulation in different combinations of multi-thin-layers under thermal gradient. Later, Koker [50] extended the equilibrium MD approach to obtain the thermal conductivity based on the kinetic conductivity relation, with phonon lifetimes, group velocities, and heat capacities by combining the first-principles MD and lattice dynamics. The thin layers in Ref. [49] were placed close to each other and no distance between the neighboring layers. Besides the Si/Ge superlattice, in the present

thesis, silicon is chosen because it serves as a principal component of most semiconductor devices, most importantly in the ICs and microchips. On the other hand, germanium is an important semiconductor material being used in transistors, solar cells [51] and other electronic devices. In addition, the silicon-germanium alloys are rapidly becoming an important semiconductor for high-speed ICs, because of the faster transmission properties of Si-SiGe junctions than the pure silicon [52].

In the chapter 3, *ab initio* MD is used to elucidate the nonequilibrium characteristics of the microstructure, translation dynamics and vibrational density of states of Si/Ge SLs during heat transfer process as the main objective. The work is performed to simulate the heat conduction occurring in the cross-plane direction of symmetrically strained Si/Ge SLs. After obtaining the trajectories, by post-processing, the temperature curves corresponding to the evolution of simulation process is plotted and further comparisons of the RDF and MSD curves of the Si/Ge layers at specified moments of the equilibration time are made. Meanwhile, analyses and discussions for the differences among the different figures are carried out to show the influences of heat transfer on the structures and dynamics of the Si/Ge SLs. Moreover, the vibrational density of states (VDOS) of the two layers are plotted and analyzed to investigate the contribution of different frequency phonons to the thermal transport efficiency.

In the chapter 4, we extend the *ab initio* MD simulation from heat conduction to thermal radiation. As aforementioned, the existence of interfacial gaps is unavoidable in reality. In this chapter, the first-principles MD simulation of the atomic-scale energy transport

from heat conduction to thermal radiation in spatial and temporal perspective is carried out. Transport phenomena occurring between silicon and/or germanium layers with gaps are investigated. In this work, thin semiconductor layers with variable gap distance with an interval of lattice constant increment of the simulated materials are set up. Comparisons of temperature evolution curves under different gaps are made. Thermal transport between the same and different kinds of materials under different temperature combinations will be investigated.

In the chapter 5, the ab initio molecular dynamics simulation method based on finite temperature (FT-DFT) is used to simulate femtosecond laser interaction of germanium. The approach has already been employed to simulate the laser melting of silicon and graphite [36,53]. Since the FT-DFT method incorporates self-consistently the effect of thermalized electronic excitations and fractionally occupied state, it can reasonably and accurately describe the electronically hot system. The original work of ab initio molecular dynamics of excited electrons was presented by Alavi *et al.* [54]. We carried out simulation with different incident laser intensities of ~ 100 fs time duration. All the cases started from germanium crystal at room temperature (300 K). To obtain the final equilibrium state of the electronic and ionic subsystem, we monitored the temperature of nucleus as output during the entire simulation process. The phase changes from the solid state to liquid state (melting point of Ge: 1211.40 K) and gas phase (evaporation point of Ge: 3106 K) were validated from the microstructure property, thermal motion and dynamics feature analysis.

Chapter 2 Theory of Ab Initio Molecular Dynamics

2.1 Born-Oppenheimer Approximation

By considering a system composed of N nuclei at positions $\{\mathbf{R}_1, \mathbf{R}_2, \dots, \mathbf{R}_N\}$ (denoted as \mathbf{R}^N) and momenta $\{\mathbf{P}_1, \mathbf{P}_2, \dots, \mathbf{P}_N\}$ (denoted as \mathbf{P}^N), and N_e electrons at positions $\{\mathbf{r}_1, \mathbf{r}_2, \dots, \mathbf{r}_{N_e}\}$ (denoted as \mathbf{r}^{N_e}) and momenta $\{\mathbf{p}_1, \mathbf{p}_2, \dots, \mathbf{p}_{N_e}\}$ (denoted as \mathbf{p}^{N_e}) and spin variables $\{s_1, s_2, \dots, s_{N_e}\}$ that described by the non-relativistic time independent Schrodinger equation

$$\mathcal{H}\Psi(\mathbf{x}^{N_e}, \mathbf{R}^N) = E\Psi(\mathbf{x}^{N_e}, \mathbf{R}^N) \quad (1)$$

where \mathbf{x}^{N_e} is denoted as the union of electronic position and spin variables. The Hamiltonian in the above equation is

$$\mathcal{H} = \sum_{I=1}^N \frac{\mathbf{P}_I^2}{2M_I} + \sum_{i=1}^{N_e} \frac{\mathbf{p}_i^2}{2m} + \sum_{i<j} \frac{e^2}{|\mathbf{r}_i - \mathbf{r}_j|} + \sum_{I<J} \frac{Z_I Z_J e^2}{|\mathbf{R}_I - \mathbf{R}_J|} - \sum_{i,I} \frac{Z_I e^2}{|\mathbf{R}_I - \mathbf{r}_i|} \quad (2)$$

where M_I is the mass of the I th nucleus and m is the mass of electron. The charge of the I th nucleus is $Z_I e$. To make it convenient in derivation, we denote the five terms (nuclear kinetic energy, the electronic kinetic energy, the electron-electron interaction, the ion-ion interaction and the electron-ion interaction) in the right side of the above equation as T_N , T_e , V_{ee} , V_{NN} and V_{eN} , respectively.

It is not possible get the exact solution of the Schrodinger equation (1), even though the systems are simple molecules. As is known to us, the motion of electrons is thousands of

time faster than that of nuclei, which means the electrons can catch up any nucleus motion at infinitesimal small time duration. In addition, the mass of nucleus is far greater than the mass of electron. Therefore, we can simplify the electron nucleus many body wavefunction into the product of nuclear and electronic wavefunction

$$\Psi(\mathbf{x}^{N_e}, \mathbf{R}^N) = \psi(\mathbf{x}^{N_e}, \mathbf{R}^N)\chi(\mathbf{R}^N) \quad (3)$$

where $\psi(\mathbf{x}^{N_e}, \mathbf{R}^N)$ is the electronic wavefunction that depends on the electronic position, spin variables and the nuclear positions. The above separation of the electronic and nuclear wavefunction is named Born-Oppenheimer approximation.

The nuclear wavefunction is more localized than the electronic wavefunction in the terms of the kinetic energy of nuclear

$$\begin{aligned} T_N[\psi(\mathbf{x}^{N_e}, \mathbf{R}^N)\chi(\mathbf{R}^N)] \\ = \frac{\hbar^2}{2} \sum_{I=1}^N \frac{1}{M_I} [\psi(\mathbf{x}^{N_e}, \mathbf{R}^N)\nabla_I^2\chi(\mathbf{R}^N)] + \chi(\mathbf{R}^N)\nabla_I^2\psi(\mathbf{x}^{N_e}, \mathbf{R}^N) \\ + 2\nabla_I\psi(\mathbf{x}^{N_e}, \mathbf{R}^N)\nabla_I\chi(\mathbf{R}^N) \end{aligned} \quad (4)$$

Hence, we can take $\nabla_I\chi(\mathbf{R}^N) \gg \nabla_I\psi(\mathbf{x}^{N_e}, \mathbf{R}^N)$ and make the simplification of equation (1) as

$$\begin{aligned} [T_e + V_{ee}(\mathbf{r}^{N_e}) + V_{eN}(\mathbf{r}^{N_e}, \mathbf{R}^N)]\psi(\mathbf{x}^{N_e}, \mathbf{R}^N)\chi(\mathbf{R}^N) + T_N\psi(\mathbf{x}^{N_e}, \mathbf{R}^N)\chi(\mathbf{R}^N) \\ + V_{NN}(\mathbf{R}^N)\psi(\mathbf{x}^{N_e}, \mathbf{R}^N)\chi(\mathbf{R}^N) = E\psi(\mathbf{x}^{N_e}, \mathbf{R}^N)\chi(\mathbf{R}^N) \end{aligned} \quad (5)$$

Furthermore, dividing $\psi(\mathbf{x}^{N_e}, \mathbf{R}^N)\chi(\mathbf{R}^N)$ on both sides

$$\frac{[T_e + V_{ee}(\mathbf{r}^{N_e}) + V_{eN}(\mathbf{r}^{N_e}, \mathbf{R}^N)]\psi(\mathbf{x}^{N_e}, \mathbf{R}^N)}{\psi(\mathbf{x}^{N_e}, \mathbf{R}^N)} = E - \frac{[T_N + V_{NN}(\mathbf{R}^N)]\chi(\mathbf{R}^N)}{\chi(\mathbf{R}^N)} \quad (6)$$

We can find the right side can be expressed as a function of \mathbf{R}^N alone. The function is denoted as $\epsilon(\mathbf{R}^N)$

$$[T_e + V_{ee}(\mathbf{r}^{N_e}) + V_{eN}(\mathbf{r}^{N_e}, \mathbf{R}^N)]\psi(\mathbf{x}^{N_e}, \mathbf{R}^N) = \epsilon_n(\mathbf{R}^N)\psi(\mathbf{x}^{N_e}, \mathbf{R}^N) \quad (7)$$

Therefore, the electronic Hamiltonian can be defined as $\mathcal{H}_e = T_e + V_{ee} + V_{eN}$. For each solution of equation (7), there will be a corresponding nuclear eigenvalue equation

$$[T_N + V_{NN}(\mathbf{R}^N) + \epsilon_n(\mathbf{R}^N)]\chi(\mathbf{R}^N) = E\chi(\mathbf{R}^N) \quad (8)$$

Transforming equation (8) into time dependent Schrodinger equation,

$$[T_N + V_{NN}(\mathbf{R}^N) + \epsilon_n(\mathbf{R}^N)]X(\mathbf{R}^N, t) = i\frac{\partial}{\partial t}X(\mathbf{R}^N, t) \quad (9)$$

which means the electrons respond instantaneously to the nuclear motion. In addition, for each nuclear configuration \mathbf{R}^N , the corresponding set of electronic eigenvalues and eigenfunctions can be obtained. In general we only consider the ground electronic surface, which is

$$[T_e + V_{ee}(\mathbf{r}^{N_e}) + V_{eN}(\mathbf{r}^{N_e}, \mathbf{R}^N)]\psi(\mathbf{x}^{N_e}, \mathbf{R}^N) = \epsilon_0(\mathbf{R}^N)\psi_0(\mathbf{x}^{N_e}, \mathbf{R}^N) \quad (10)$$

By neglecting the quantum effects for the description of the nuclear motion, assuming $X(\mathbf{R}^N, t) = A(\mathbf{R}^N, t)e^{iS(\mathbf{R}^N, t)/\hbar}$ and then neglecting all terms involving \hbar (the classical extreme), we obtain the classical Hamilton-Jacobi equation in terms of the classical nuclear Hamiltonian

$$\mathcal{H}_N(\mathbf{P}^N, \mathbf{R}^N) = \sum_{I=1}^N \frac{\mathbf{P}_I^2}{2M_I} + V_{NN}(\mathbf{R}^N) + \epsilon_0(\mathbf{R}^N) \quad (11)$$

Therefore, we can get the potential term

$$E_0(\mathbf{R}^N) = V_{NN}(\mathbf{R}^N) + \epsilon_0(\mathbf{R}^N) \quad (12)$$

The classical motion of nuclei at ground state is

$$\begin{aligned} \dot{\mathbf{P}}_I &= -\nabla_I E_0(\mathbf{R}^N) \\ \dot{\mathbf{R}}_I &= \frac{\mathbf{P}_I}{M_I} \end{aligned} \quad (13)$$

The right side in equation (13) implies the force acting on nucleus contains a term from the ion-ion interaction $V_{NN}(\mathbf{R}^N)$ and a term from the derivative of the electronic eigenvalue $\epsilon_0(\mathbf{R}^N)$. The quantum molecular dynamics that employs the Born-Oppenheimer approximation is called Born-Oppenheimer molecular dynamics (BOMD).

Recall the Hellmann Feynman theorem, $\nabla_I \epsilon_0(\mathbf{R}^N)$ in equation (13) can be expressed as

$$\nabla_I \epsilon_0(\mathbf{R}^N) = \langle \Psi_0(\mathbf{R}^N) | \nabla_I \mathcal{H}_e(\mathbf{R}^N) | \Psi_0(\mathbf{R}^N) \rangle \quad (14)$$

Equations (13) and (14) are the fundamental theory in ab initio molecular dynamics simulation. In ad initio molecular dynamics calculation, we have to get the numerical solution of equation (13) by computing the forces of from equation (14) at each time step. In each BOMD time step, the minimization of $\mathcal{H}_e(\mathbf{R}^N)$ has to be calculated.

2.2 Density Functional Theory

When it comes to ab initio molecular dynamics simulation, let's focus on the Kohn-Sham method of density functional theory firstly [55]. According to the Kohn-Sham (KS) theory, the difficult many-body system can be replaced with an independent particular system, which leads to the ground state energy of the interacting system of electrons with classical nuclei at position $\{\mathbf{R}_{n,I}\}$ into a set of orthonormal one particle functions.

$$\min_{\Psi_0} \{\langle \Psi_0 | \mathcal{H}_e | \Psi_0 \rangle\} = \min_{\{\boldsymbol{\varphi}_i\}} E^{KS} \{\boldsymbol{\varphi}_i(\mathbf{r})\} \quad (15)$$

where $\boldsymbol{\varphi}_i(\mathbf{r})$ are known as the Kohn-Sham orbitals.

The minimized Kohn-Sham energy [56] can be expressed as:

$$E_{min}^{KS}[\{\boldsymbol{\varphi}_i\}] = T_s[\{\boldsymbol{\varphi}_i\}] + E_{ext} + E_H + E_{xc}[n] + E_{ions}(\mathbf{R}^N) \quad (16)$$

where T_s , E_{ext} , E_H , E_{xc} and $E_{ions}(\mathbf{R}^N)$ denote the kinetic energy $\sum_i^{occ} f_i \left\langle \boldsymbol{\varphi}_i \left| -\frac{\hbar^2}{2m} \nabla^2 \right| \boldsymbol{\varphi}_i \right\rangle$, the electron-ion energy $-\sum_I \frac{Z_I e^2}{|\mathbf{R}_I - \mathbf{r}|}$ (which characterizes the energy due to the interaction with an external potential), the classical Hartree energy $\frac{e^2}{2} \int \left(\int \frac{\rho(\mathbf{r}')}{|\mathbf{r} - \mathbf{r}'|} d\mathbf{r}' \right) \rho(\mathbf{r}) d\mathbf{r}$ (which refers the classical electrostatic energy of two charge clouds), the exchange and correlation energy and the ion-ion Coulombic interaction $\sum_{I < J} \frac{Z_I Z_J e^2}{|\mathbf{R}_I - \mathbf{R}_J|}$ among the nuclei, respectively. The electronic charge density is $\rho(\mathbf{r}) = \sum_i^{occ} f_i |\boldsymbol{\varphi}_i(\mathbf{r})|^2$. Considering the orthonormality of electronic orbitals, we denote the extended KS energy $E^{KS} - \sum_{ij} \Lambda_{ij} (\langle \boldsymbol{\varphi}_i | \boldsymbol{\varphi}_j \rangle - \delta_{ij})$ as ε^{KS} for simplicity. The matrix Λ_{ij} here refers a set of multipliers introduced for the purpose of ensuring the condition $\langle \boldsymbol{\varphi}_i | \boldsymbol{\varphi}_j \rangle = \delta_{ij}$.

2.3 Car-Parrinello Molecular Dynamics

In the chapter 3 and 4, we performed ab initio MD simulations using Car-Parrinello scheme [57], which uses the density functional theory (DFT) to derive the interatomic force constants. As given in section 2.1, there are no electron dynamics involved in solving the equation of nuclear motion in BOMD. However, a high computational load is introduced by solving the electronic structure problem self consistently at each MD step. Therefore, the CPMD is chosen not only it bears the advantage of being free from the empirical parameters and its general applicability, but also it cuts the computational expenses of BOMD by simplifying the electrons in a single state. The significant difference that distinguishes the CPMD from BOMD is the introduction of a fictitious dynamics for electronic degrees of freedom. In CPMD, because of the introduced fictitious electronic dynamics, the electronic wavefunction is kept automatically minimized to its ground state along with the propagation of nuclei. Consequently, it reduces the computational load of CPMD comparing with BOMD that needs to solve the electronic wavefunction self-consistently at each MD step.

The CPMD method has already been described elsewhere [57–59] in detail. Here we limit ourselves to recall the fundamental and brief derivation of the simulation method from the classical MD to the first-principles MD. More detailed theoretical framework of Car-Parrinello molecular dynamics can be found in the original work [60].

Similar to the N atoms system introduced in section 2.1, let's consider the atoms vibrating under the influence of a potential. The potential U is a function of the positions

only, is denoted as $U(\mathbf{R}^N)$. Thus, the system can be expressed in terms of Lagrangian equation

$$\mathcal{L}(\mathbf{R}^N, \dot{\mathbf{R}}^N) = \sum_{I=1}^N \frac{1}{2} M_I \dot{\mathbf{R}}_I^2 - U(\mathbf{R}^N) \quad (17)$$

The associated Euler-Lagrange equation is

$$\frac{d}{dt} \frac{\partial \mathcal{L}}{\partial \dot{\mathbf{R}}_I} = \frac{\partial \mathcal{L}}{\partial \mathbf{R}_I} \quad (18)$$

As introduced before, the distinct difference between classical MD and CPMD is the source of potential. In the classical MD, the empirical potential functions are usually obtained by curve fitting method under prescribed conditions [61] or from experimental approaches [62]. Because of the transferability and accuracy of empirical potential, together with its failure to take full account for influence of electrons in the classical MD, the simulation results may not objectively reflect and reveal fundamental chemo-physical process comparing with the ab initio MD.

In classical mechanics, the force on nuclei is obtained from the derivate of Lagrangian with respect to nuclear positions. Similarly, by considering the extended KS energy function ε^{KS} to be dependent on \mathbf{R}^N and $\boldsymbol{\varphi}_i$. Car and Parrinello postulated a Lagrangian functional derivative with respect to the orbitals [57], which can also be interpreted as classical force fields:

$$\mathcal{L}_{CP}[\mathbf{R}^N, \dot{\mathbf{R}}^N, \{\boldsymbol{\varphi}_i\}, \{\dot{\boldsymbol{\varphi}}_i\}] = \sum_I \frac{1}{2} M_I \dot{\mathbf{R}}_I^2 + \sum_i \frac{1}{2} \mu_i \langle \dot{\boldsymbol{\varphi}}_i | \dot{\boldsymbol{\varphi}}_i \rangle - \varepsilon^{KS}[\{\boldsymbol{\varphi}_i\}, \mathbf{R}^N] \quad (19)$$

where the atomic mass is denoted as M_I , the nuclear degree of freedom is denoted as $\dot{\mathbf{R}}_I$, and the electronic one-particle orbital is denoted as $\boldsymbol{\varphi}_i$. μ_i is the fictitious mass or inertia parameter assigned to the orbital degree of freedom. During the CPMD simulation process, the electrons are kept at a much lower fictitious electronic temperature comparing with the nuclear temperature, in order to make sure that the electronic subsystem is close to its instantaneous minimum energy. Consequently, under certain postulation of fictitious kinetic energy of electrons, the electrons are kept on the surface of Born-Oppenheimer surface and there is no energy transfer between the nuclei with high temperature and electrons with low temperature.

By transforming from the quantum mechanical time-scale separation of fast electronic and slow nuclear motion into a classical mechanical adiabatic energy scale separation in the frame work of dynamical system theory, the potential (force) required in CPMD simulation is the partial derivative of the Kohn-Sham energy with respect to independently variables $\boldsymbol{\varphi}_i$ and \mathbf{R}^N . Therefore, the corresponding Car-Parrinello equations of motion are obtained from the associated Euler-Lagrange equations:

$$M_I \ddot{\mathbf{R}}_I(t) = -\frac{\partial \varepsilon^{KS}}{\partial \mathbf{R}_I} = -\frac{\partial [E^{KS} - \sum_{ij} (\langle \boldsymbol{\varphi}_i | \boldsymbol{\varphi}_j \rangle - \delta_{ij})]}{\partial \mathbf{R}_I} \approx -\frac{\partial E^{KS}}{\partial \mathbf{R}_I} + \sum_{ij} \Lambda_{ij} \frac{\partial \langle \boldsymbol{\varphi}_i | \boldsymbol{\varphi}_j \rangle}{\partial \mathbf{R}_I} \quad (20)$$

$$\mu_i \ddot{\boldsymbol{\varphi}}_i(t) = -\frac{\delta \varepsilon^{KS}}{\delta \langle \boldsymbol{\varphi}_i |} = -\frac{\delta [E^{KS} - \sum_{ij} (\langle \boldsymbol{\varphi}_i | \boldsymbol{\varphi}_j \rangle - \delta_{ij})]}{\delta \langle \boldsymbol{\varphi}_i |} \approx -\frac{\delta E^{KS}}{\delta \langle \boldsymbol{\varphi}_i |} + \sum_j \Lambda_{ij} | \boldsymbol{\varphi}_j \rangle \quad (21)$$

Because the term $\sum_i \left[\frac{\partial E^{KS}}{\partial \mathbf{R}_I} + \sum_j \Lambda_{ij} | \boldsymbol{\varphi}_j \rangle \right]$ in $-\frac{\partial \varepsilon^{KS}}{\partial \mathbf{R}_I}$ is almost zero in Eq. (5), and so is in Eq. (6), the simplification of " \approx " is obtained. According to Eqs. (5) and (6), the idea of getting the time scale separation of fast electronic and slow nuclear motion is realized by transforming that into classical mechanical adiabatic energy scale separation in the

framework of DFT. Therefore, the simultaneous time evolution of both the ionic and the electronic degrees of freedom can be determined by integrating Eq. (5) and (6).

In CPMD code, plane wave / pseudopotential method is employed in the simulation algorithm. In a modeled system, a periodically repeated unit cell is defined by using the lattice vectors \mathbf{a}_1 , \mathbf{a}_2 , and \mathbf{a}_3 . Combining with the scaled coordinates s , we can express the established system as

$$\mathbf{r} = s\mathbf{h} = s[\mathbf{a}_1 \quad \mathbf{a}_2 \quad \mathbf{a}_3] \quad (22)$$

Reciprocal lattice vectors \mathbf{b}_i are defined as

$$\mathbf{b}_i \cdot \mathbf{a}_j = 2\pi\delta_{ij} \quad (23)$$

Periodic boundary condition are established by using

$$\mathbf{r}_{pbc} = \mathbf{r} - \mathbf{h}[\mathbf{h}^{-1}\mathbf{r}]_{NINT} \quad (24)$$

where $[\mathbf{h}^{-1}\mathbf{r}]_{NINT}$ is the nearest integer value. With the assumed periodicity, an orthonormal basis is built by plane waves as

$$f_G^{PW}(\mathbf{r}) = \frac{1}{\sqrt{\Omega}} e^{i\mathbf{G}\cdot\mathbf{r}} = \frac{1}{\sqrt{\Omega}} e^{2\pi i\mathbf{g}\cdot s} \quad (25)$$

where Ω is the volume of the unit cell. \mathbf{G} is the reciprocal space vectors $2\pi(\mathbf{h}^t)^{-1}\mathbf{g}$ and \mathbf{g} refers a triple of integer values. Furthermore, a periodic function can be expanded in the basis as

$$f_G^{PW}(\mathbf{r}) = f_G^{PW}(\mathbf{r} + \mathbf{L}) = \frac{1}{\sqrt{\Omega}} \sum_{\mathbf{G}} e^{i\mathbf{G}\cdot\mathbf{r}} \quad (26)$$

The real vectors and the reciprocal vectors relate from each other by the three dimensional Fast Fourier Transform.

The Kohn-Sham orbitals can be expressed in Bloch form:

$$\boldsymbol{\varphi}_{i\mathbf{k}}(\mathbf{r}) = e^{i\mathbf{k}\cdot\mathbf{r}}u_{i\mathbf{k}}(\mathbf{r}) \quad (27)$$

where \mathbf{k} is a vector in the first Brillouin zone and $u_{i\mathbf{k}}(\mathbf{r})$ is a periodic function that can be expanded as the sum of a series plane wave basis set $\frac{1}{\sqrt{\Omega}}\sum_{\mathbf{G}}c_i^{\mathbf{k}}(\mathbf{G},\mathbf{k})e^{i\mathbf{G}\cdot\mathbf{r}}$ ($c_i(\mathbf{G},\mathbf{k})$ are the expansion coefficients). For the system considered in this thesis is nonmetallic, only the single point $\mathbf{k} = [0 \ 0 \ 0]$ (the Γ point) is taken. Therefore, the plane wave expansion becomes

$$\boldsymbol{\varphi}_{i\mathbf{k}}(\mathbf{r}) = \frac{1}{\sqrt{\Omega}}\sum_{\mathbf{G}}c_i(\mathbf{G},\mathbf{k})e^{i\mathbf{G}\cdot\mathbf{r}} \quad (28)$$

In practical simulation, the infinite sum over the reciprocal space \mathbf{G} has to be truncated. The truncation should meet the criteria that the Kohn-Sham potential converges rapidly. The cutoff is chosen in simulation should be larger than the kinetic energy with \mathbf{G} vectors. Namely

$$E_{cut} \geq \frac{1}{2}|\mathbf{G}|^2 \quad (29)$$

The number of plane waves is defined

$$N^{PW} \geq \frac{1}{2\pi^2}\Omega E_{cut}^{3/2} \quad (30)$$

Plane waves represent the periodic part of the orbitals in form of basis set, which realizes the purpose that the periodic lattice produces a periodic potential and then imposes the same periodicity on the density.

The employment of pseudopotential approach provides an effective and feasible way to performing calculations on the complex systems (liquid and solid state) using plane wave basis sets. In the framework of pseudopotential, the chemically active valence electrons are taken into account explicitly and the inert core electrons are eliminated as a “frozen state” together with the nuclei. The pseudopotentials have to correctly represent the long range interactions of the core. In addition, the produced pseudo-wavefunctions should get the equal accuracy as the full wavefunction calculations. The properties of additivity and transferability should be satisfied for the pseudopotentials. Thus, the purpose of obtaining smooth pseudo orbitals to describe the valence electrons and keeping the core and valence states orthogonal in an all electron framework is realized.

2.4 Ab Initio Molecular Dynamics with Excited Electrons

In the simulation of femtosecond laser lithography in Chapter 5, we used the FT-DFT to perform ab initio molecular dynamics with excited electrons. The concept of finite temperature version of the density functional theory was originally proposed by Mermin [63] when it referred to the thermal properties of electron gas. The functional introducing the finite electron temperature of effects into the DFT is

$$\Omega[\boldsymbol{\varphi}_i(\mathbf{r})] = E^{KS}[\boldsymbol{\varphi}_i(\mathbf{r})] - T_e S \quad (31)$$

where $E^{KS}[\boldsymbol{\varphi}_i(\mathbf{r})]$ is the Kohn-Sham energy functional at $T_e = 0$. S is the entropy which can be expressed as

$$S = -k_B \sum_i [f_i \ln f_i + (1 - f_i) \ln(1 - f_i)] \quad (32)$$

For the specific case of non-interacting Fermions, the grand potential expression is

$$\Omega(\mu VT) = -k_B T \det^2(1 + e^{-\beta(\mathcal{H} - \mu)}) \quad (33)$$

where μ refers to the chemical potential acting on the electrons and \mathcal{H} is the one electron Hamiltonian $\mathcal{H} = -\frac{\hbar^2}{2m} \nabla^2 + V(\mathbf{r})$. The power of two is because of the spin multiplicity.

The effective density dependent potential term in Hamiltonian is expressed as

$$V(\mathbf{r}) = - \sum_I \frac{Z_I e^2}{|\mathbf{R}_I - \mathbf{r}|} + V_H + \frac{\delta \Omega_{xc}}{\delta \rho(\mathbf{r})} \quad (34)$$

The free energy \mathcal{F} is a functional of the electron density $\rho(\mathbf{r})$, the Fermi-Dirac occupation number f_i of the one-electron eigenstates $\boldsymbol{\varphi}_i(\mathbf{r})$ and the chemical potential μ .

Recalling the mathematical relationship $\left(\frac{\partial \Omega}{\partial \mu}\right)_{\rho(\mathbf{r})} = -N$ in thermodynamics, we can get

the average electron number. Therefore, the sum of the Helmholtz free energy [54] of one electron of density $\rho(\mathbf{r})$ and the ion-ion Coulomb energy $E_{ions}(\mathbf{R}^N)$:

$$\mathcal{F} = \Omega + \mu N_e + E_{ions}(\mathbf{R}^N) \quad (35)$$

where Ω denotes the grand potential for an interacting spin Fermi gas within DFT. In order to obtain the correct total electronic free energy of the interacting electrons, the extra terms have to be included in Ω^{KS} , namely

$$\Omega = -\frac{2}{\beta} \ln \det(1 + e^{-\beta(\mathcal{H}-\mu)}) - V_H - \int \rho(\mathbf{r}) \left(\frac{\delta \Omega_{xc}}{\delta \rho(\mathbf{r})} \right) d\mathbf{r} + \Omega_{xc} \quad (36)$$

where $\beta = \frac{1}{k_B T_e}$ refers to the electron temperature parameter and Ω_{xc} is the finite temperature exchange correlation grand potential functional.

The density

$$\rho(\mathbf{r}) = \sum_i^{occ} f_i(T) |\boldsymbol{\phi}_i(\mathbf{r})|^2 \quad (37)$$

and

$$f_i(T) = \frac{f_i(0)}{1 + e^{-\frac{1}{k_B T_e}(\epsilon_i^{KS} - \mu)}} \quad (38)$$

where ϵ_i^{KS} is the Kohn-Sham eigenvalues and $f_i(T)$ is the Fermi-Dirac occupation number in the grand canonical ensemble.

The optimization for the specific atomic configuration can be realized by adopting the Lanczos algorithm [64]. After the computed electron density $\rho(\mathbf{r})$ is obtained, the dynamic simulation is performed based on the optimization of the electronic density at every time step. Then, the Hellmann-Feynman forces acting on the nuclear can be calculated via the differentiation of \mathcal{F} with respect to the ionic coordinates.

$$\mathbf{F}_I = -\nabla_I \mathcal{F} \quad (39)$$

Eventually, we can perform molecular dynamics simulation for the system with various temperatures of electrons.

Chapter 3 Car-Parrinello MD Study of Structural, Dynamic, and Vibrational Properties of Si/Ge Superlattices during Heat Transfer

3.1 Modeling and Simulation

The ab initio MD calculations were carried out based on the plane-wave pseudopotential implementation of density functional theory, which is written in the latest CPMD package version 3.15.3 [65]. We established a supercell that contains atoms $4(\text{width}) \times 4(\text{length})$ as the cross section basis and 8 atoms equally assigned for each layer (as is shown in Fig. 1 by VMD [66]).

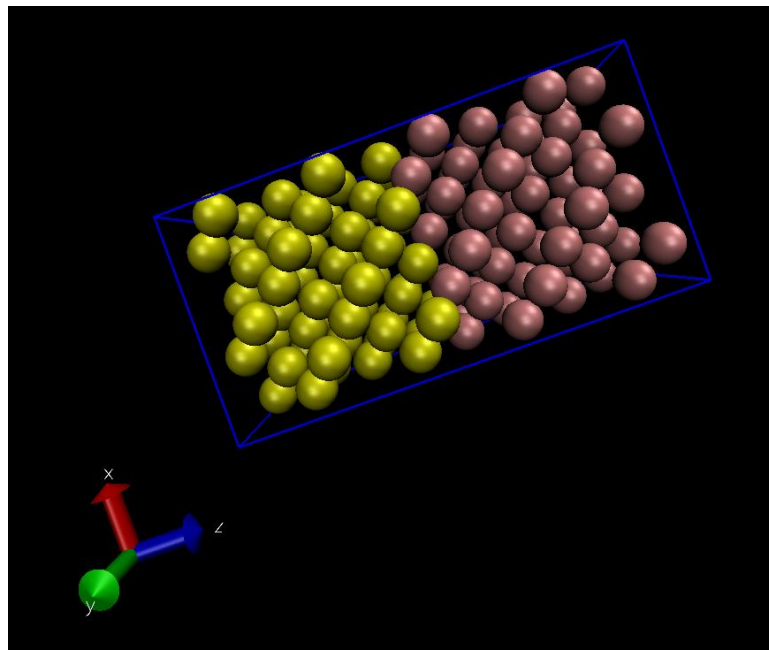


Fig. 1 Supercell for the Si/Ge superlattices modeling

For the sub-model of silicon layer, we set the lattice constant as 5.431 \AA [67] in the Cartesian coordinate system, while for the sub-model of germanium layer, the lattice constant was 5.568 \AA [68]. Both the silicon and germanium have zinc-blende structure. Because the parameters of the supercell are set 11.316 \AA for the length of the cross-section square and 22.632 \AA in the height, the neighboring Si/Ge layers can be regarded as closely attached to each other. Furthermore, the same kind of lattice structure makes the interface match well. The lattice structure of Si and Ge are both diamond cubic and the two layers are in direct contact (without any gap separating the layers). Therefore, we can treat the heat transfer process as heat conduction, rather than radiation. To simulate the alternating super-thin layers of silicon and germanium, we employed periodic boundary conditions in all three directions during the entire simulation process. A schematic view of the Si/Ge superlattices is shown in Fig. 2.

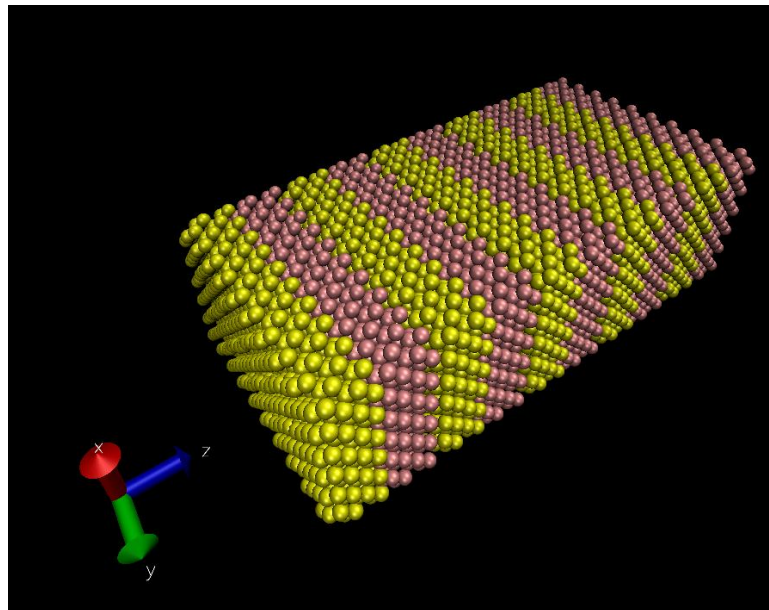


Fig. 2 Periodically alternating Si/Ge superlattices

To start the CPMD simulation, wavefunction optimization of the system was the first step and further MD simulations were based on the optimized system. If a MD simulation is executed from a non-converged wavefunction, in the consequent work, the electrons maybe far away from the Born-Oppenheimer surface and the results produced will be unphysical. In our simulation, the CPMD calculations were executed based on the LDA of the exchange-correlation functional augmented by Becke–Lee–Yang–Parr (BLYP) [69,70] generalized gradient corrections. The valence electrons were treated explicitly and electron-ion interactions were described by norm-conserving pseudopotentials generated. We chose the Trouiller-Martins [71] norm-conserving nonlocal pseudopotentials to represent the core electrons for both silicon and germanium and the maximum l – quantum numbers were set as P. The Kohn-Sham orbitals had the periodicity of the supercell and were expanded in plane waves up to a kinetic energy cutoff of 30 Ry. The Γ point [$k = (0, 0, 0)$] was used to sample the Brillouin zone of MD supercell. After obtaining the optimized wavefunction and geometry, the electronic degrees of freedom were quenched to the Born Oppenheimer surface. We started the CPMD simulation with NVT ensemble adopted to form the steady non-equilibrium state with a time step of 4.0 *a.u.* (about 0.096,755 *fs*) to integrate the equations of motion, which was found to produce a satisfactory convergence in the wavefunction and geometry optimization. To keep the constant temperatures of the layers, silicon 800 *K* and germanium 300 *K*, the Nose-Hoover thermostats [72] were imposed on ions and electrons (with a fictitious electronic mass of 400 *a.u.*) for each degree of freedom. We

ran the NVT simulation for 20,000 time steps to make sure that the layers had sufficient time to reach steady states, which meant that the temperatures differences are well established for the layers. Then, the thermostats were removed and the system was set adiabatically to launch the NVE simulation. It came to the most crucial point to keep the total energy of the two layers conserved and let the two sorts of thermal gradients evolve smaller and smaller spontaneously. The vibrations of atoms varied with the heat flow from silicon layer to germanium layer. During the entire CPMD simulation, atomic configurations and velocities were saved in every time step, then we extracted the trajectories at different time ranges and perform statistical computations of the RDF and MSD based on the program ISAACS [73]. In addition, the overall temperature curves of the two layers were plots with the evolution of simulation time. In the end, the normalized vibration spectra were also calculated as a supplementary part to probe the resonance mode of the two layers' thermal communication.

3.2 Results and Discussion

3.2.1 Temperature Evolutions with Simulation Time Steps

We calculated the temperatures of the two layers along with the proceeding of MD simulation and plotted the two temperature curves corresponding to the simulation time steps of the silicon and germanium layers, respectively. The temperatures are defined according to the kinetic theory by taking mean kinetic energy over all Si/Ge atoms in three directions. There are two purposes to monitor the temperature variations: (1) the

temperature curves reflect general thermal states of the two layers and their difference, and (2) we can determine the moment to terminate the simulation at the point which the two temperature curves converges.

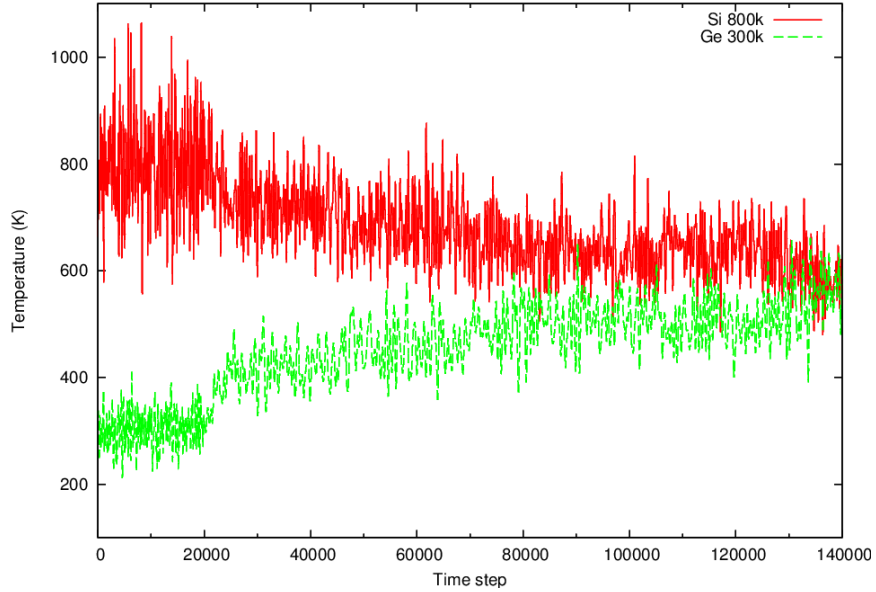


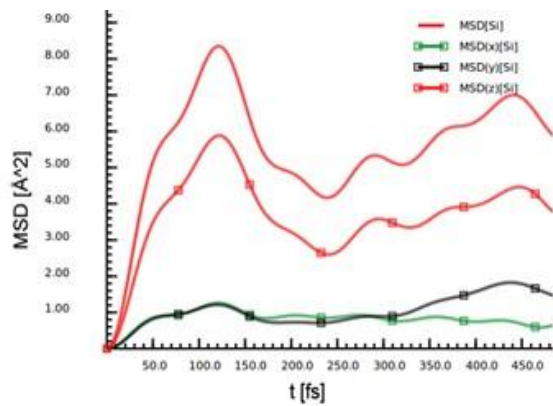
Fig. 3 Temperature evolution curves obtained from MD simulation

As is shown in Fig. 3, at the first 20,000 time steps with the thermostats clapped on both layer, the temperate profiles oscillate around 800 K for silicon layers and 300 K for germanium layers. The oscillation magnitudes are inversely proportional to the square root of the numbers of atoms included in the calculation of the mean temperatures of the silicon and germanium subsystems. Since the mean temperature of silicon layer is higher than that of germanium layer, oscillation for silicon curve is reasonably more significant. After releasing the thermostats, heat conduction occurs due to the temperature gradient between the neighboring layers and the equilibration time is about 11.320 ps (117,000 time steps). In solid materials, the heat conduction process is interpreted as the vibrations of atoms coupling from each other form waves of atomic displacements. Phonon is

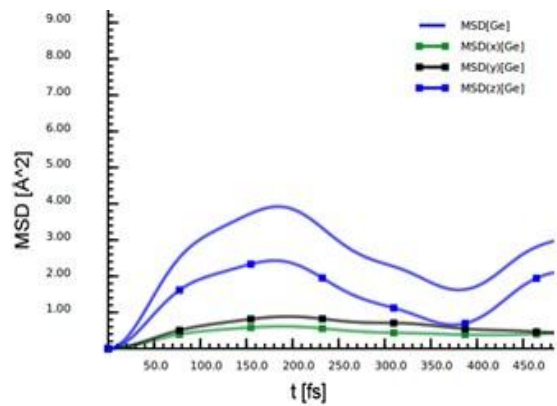
defined by the product of the vibrational frequency ν with the Planck constant h , which is the smallest quantized vibrational energy. The overall motions of atoms form the elastic waves that convey the thermal energy from one site to the other. As for semiconductors, due to the fact that the free electron density is much lower than that in metal, the contribution of electrons in thermal energy transport is neglected. By calculating under the framework of DFT theory, we can get accurate force constants acting on the atoms and then predict the motion of atoms. According to definition of phonon, one kind of spatially localized, quantized units of propagating vibration wave, one can associate the characteristic of phonons with the motions of atoms included in the trajectories obtained from MD simulation. As reported by Luo and Lloyd [74] equilibration time for silicon-germanium-layer (750 K versus 450 K) with the thickness of 5.658 Å is 12.772 ps (132,000 time steps), which is close to the simulation result 11.320 ps in the current work.

3.2.2 Translation Dynamics at Different Simulation Stages

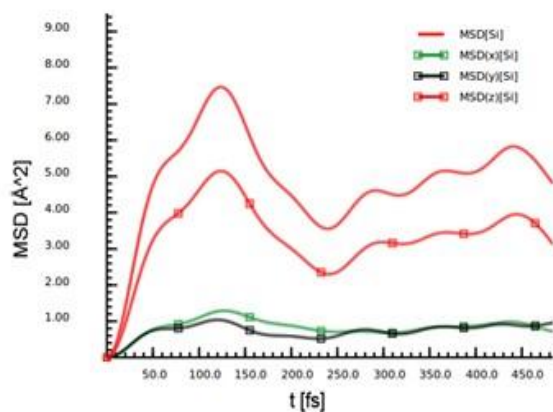
We calculated the overall MSD and the directional MSD for the two layers at different simulation stages at the same sampling points as those of RDA in Section 4.2.1. The MSD plots are illustrated in Fig. 4 with a sampling time range of 483.775 fs (5,000 time steps). The profiles of the plotted MSD agree with the ones reported in [75].



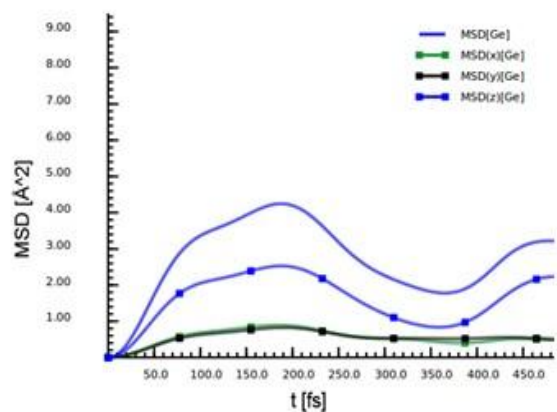
a (Si)



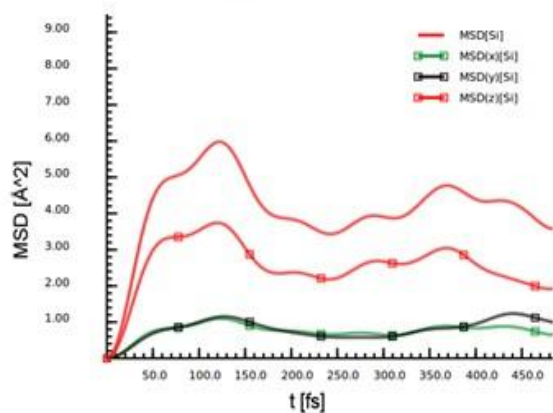
a (Ge)



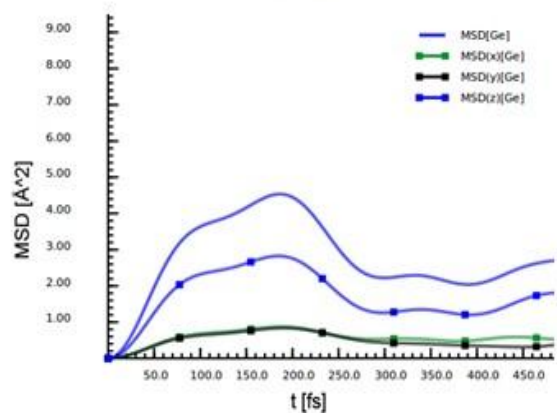
b (Si)



b (Ge)



c (Si)



c (Ge)

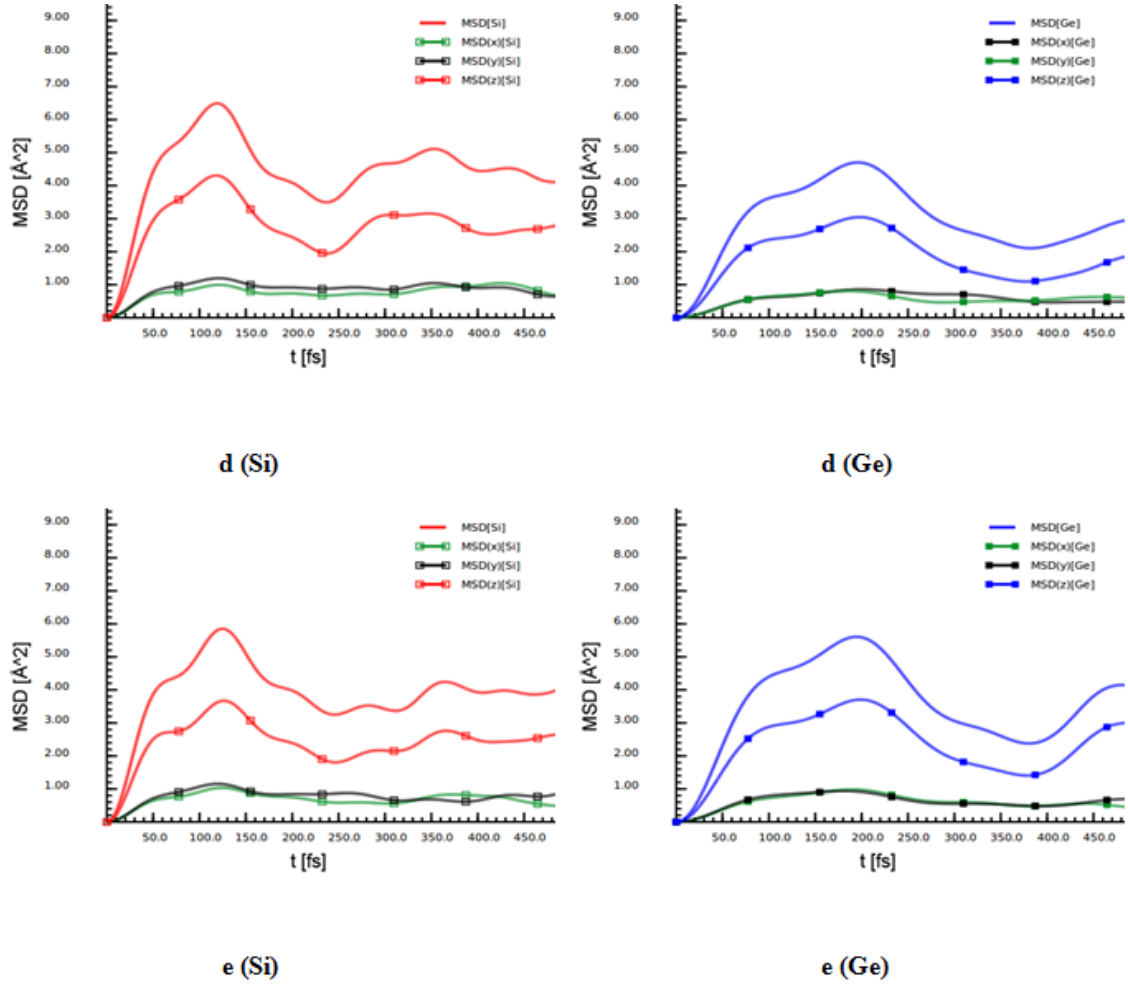


Fig. 4 MSDs in different simulation stages

Since the temperature of the silicon layer (800 K) is greater than that of the germanium layer (300 K), the distance of motion at each time should be longer for silicon atoms. The other aspect we should pay attention to is the significantly great value of MSD in z direction than the other two directions (x and y) and it almost has the same profile as the overall MSD. Since we set the dimensions for each layer with equal lengths and the layers are composed of $4 \times 4 \times 4$ atoms, the internal energy is equally distributed in the three dimensions. Considering the fact that the two layers are stacked alternatively in the z - direction, the only explanation for the greater of MSD in the z - direction that it is caused by the non-equilibrium thermal states. The overall MSD is dominated by the z -

direction displacements of the atoms. Comparing the curves among the Figs. 4(a)-5(e), we can conclude that the MSDs for germanium layer gradually become higher while the MSDs for silicon layer render a tendency of lower and lower. It indicates the atoms' displacements change agree well with the temperatures evolution. As it is shown in Fig. 4(e), at the final dynamic equilibrium stage with nearly equivalent amount of thermal energy absorption and emission, compared with curves in Fig. 4(d), the MSD values for silicon gets lower and germanium gets greater. But due to the mass difference of silicon and germanium atoms, the overall MSD of silicon should be greater than that of germanium.

3.2.3 Vibrational Density of States Analyses

Thermal properties, such as the heat capacity and thermal conductivity as well as some other kinds of material properties are strongly impacted by the vibrational density of states (VDOS). Hence, to get a profound grasp of the laws governing the vibrational properties of superlattices is of high technological and fundamental interest. To gain a further insight into the heat conduction process between the neighboring layers, we calculated the VDOS or the power spectra by performing the Fourier transformation of the velocity autocorrelation function. Fig. 5 shows the distribution of normalized power density versus the vibration frequency (arbitrary unit, a.u.).

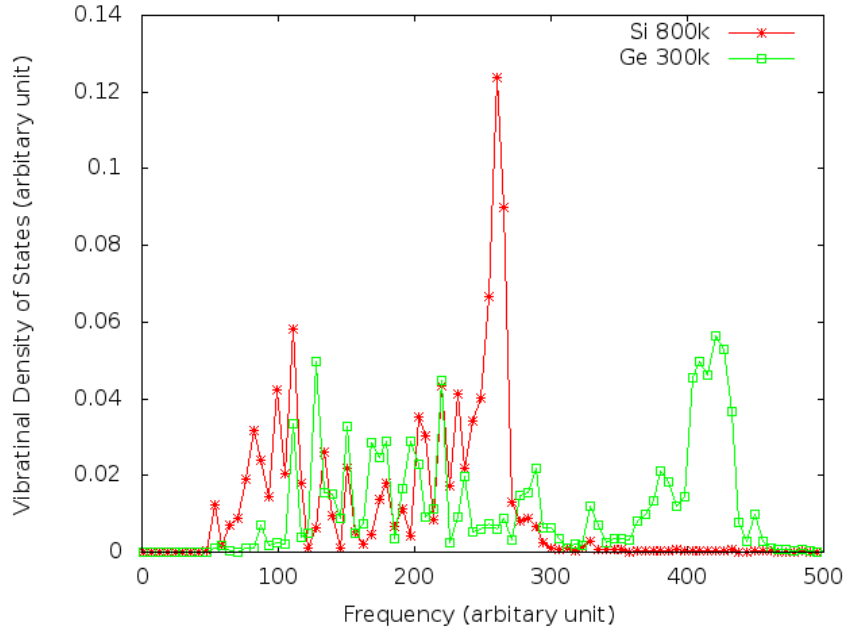


Fig. 5 Vibration spectra of the simulated Si/Ge superlattices

A comparison of VDOS for experiment and computer simulation can be found in [76]. The distinguishable peaks of silicon and germanium corresponding to high frequency vibrational modes are isolated distribute in the 250 a.u. and 430 a.u., respectively. The strong peaks lose height rapidly and the densities of distribution are relatively smaller than those in lower frequency region. From the vibration point of view, due to the mass difference, the maximum VDOS value of Si (in middle frequency region) is independent from that of Ge in high frequency region. Nevertheless, there are still some VDOS overlapping areas existing in the in the frequency range of 100 – 250 a.u., which demonstrates in thermal communication occurring between the neighboring layers inside the superlattices. As discussed in section 4.1, because of the difference of the materials, it will cause acoustic mismatch. If we take the superlattices as composite, phonon transport across the interface is incoherent. It makes the phonon scattering at the layer interface. Luckyanova *et. al* [77] showed that the anharmonic and interface rates at different

frequencies and the interfacial scattering of high frequency phonons led to a reduction in their heat carrying ability and directly induced the overall decrease in the thermal conductivity of superlattices. However, the phonon transport can also be treated as coherent if we regard the superlattices as a “homogeneous” material. In the Casimir classical size effect regime, broadband phonons are excited at one boundary and then traverse the internal region of the film ballistically before reaching the boundary of the layers. Thus, phonon propagation is coherent inside the layer. When the vibrational phonons encounter the interface between the neighboring layers, the overlapping areas in the low frequency region of VDOS make it clear that such kind of vibrational phonons locating in low frequency region are the mainly contributors to facilitate the heat transfer. Thus, there is also a proportion of the phonon energy can be coherently delivered to the neighboring layer. Namely, the interfacial heat transfer is coherent phonon heat conduction coexisting with incoherent phonon heat conduction. The proportion of coherent heat transfer has also already been discovered and investigated by Luckyanova *et al.* [77] with both experimental support and simulations verification. To interpret the mechanism in a physical point of view, the low frequency phonons corresponds with long mean free paths and therefore enable the phonons propagate longer distance through the layer interfaces.

Chapter 4 Car-Parrinello MD Simulation of Atomic Scale

Energy Transport: From Heat Conduction to Thermal Radiation

4.1 Modeling and Simulation Details

With the rapid development of cutting edge thin film growth technology, it is possible to arrange different materials at the atomic level and to fabricate the thin-film structures with strong size-effect from angstroms to hundreds nanometers. In this work, the numbers of atoms with $4(\text{length}) \times 4(\text{width})$ were built into square layers of 2 (thickness) atoms aligning in the third direction for each layer. Periodic boundary conditions were applied in all three dimensions. In the case of silicon-silicon-layer combination, the lattice constant of 5.431 \AA was used in the Cartesian coordinate modeling setting up. In the case of silicon-germanium-layer combination, the change was lattice constants of 5.431 \AA for silicon and 5.658 \AA for germanium, respectively. Both the silicon and germanium are diamond cubic crystal structure, which is a repeating pattern of 8 atoms. To take a general integration of adjacent layers ($4(\text{length}) \times 4(\text{width}) \times (2 + 2)(\text{thickness})$) and the gap discrete layers ($4(\text{length}) \times 4(\text{width}) \times (2 + 2 + x)(\text{thickness})$), where x refers to the ratio of gap distance to lattice constant), the supercell symmetry was set as orthorhombic. Fig. 7 (rendered using VMD [66]) shows the silicon-germanium-layer combination with an interfacial distance equaling to the germanium lattice constant.

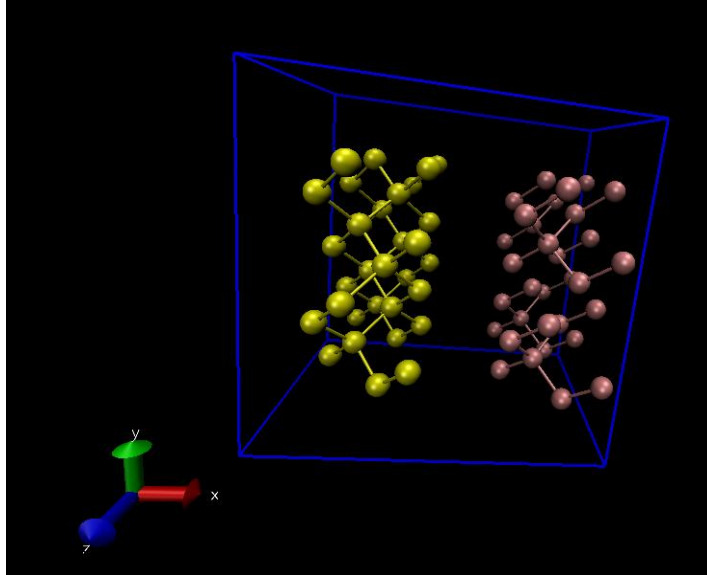


Fig. 6 Simulation box of silicon-germanium-layer combination with the Interfacial distance equals the lattice constant of germanium

Our simulations were based on the latest CPMD v.3.15.3 [65]. Each MD simulation case started from the wavefunction and geometry optimization to perform electron structure calculation of the ensemble to make sure that the consequent CPMD simulation physically runs near the Born-Oppenheimer surface. Simulation time step was set to be 4.0 a.u. ($1 \text{ a.u.} = 0.024,188,842,8 \text{ fs}$). At the first temperature control stage, canonical or NVT ensemble was employed to ensure the ensemble has a well-defined temperature. Nose-Hoover thermostats [72] were imposed on ions and electrons for each degree of freedom. The energy of endothermic and exothermic processes was exchanged with the clapped thermostats. Characteristic frequency of electrons and ions were chosen to be 10,000 and 2,500, respectively. After the temperature of the entire system reaching to steady-state, thermostats were removed to keep the system as a microcanonical or NVE ensemble and an adiabatic stage started to take place with no heat exchange between the system and its boundary. The only process was the exchange of potential and kinetic

energy inside the ensemble, with total energy being conserved. The norm-conserving pseudopotentials were used for minimizing the size of the plane wave basis to generate the same charge density as the real full electrons. The Trouiller-Martins [78] and Stumpf-Gonze-Scheffler [79] pseudopotentials were used for silicon and germanium layers, respectively. The thermal energy exchange between the neighboring layers and potential energy of atoms in the layers would be considered. In the cases of interfacial distance varying with an interval of lattice constant increment of simulated materials, because the gaps between layers can be regarded as vacuum, and the thermal energy exchange is realized from heat conduction to thermal radiation.

4.2 Results and Discussion

4.2.1 Pure Material Combinations

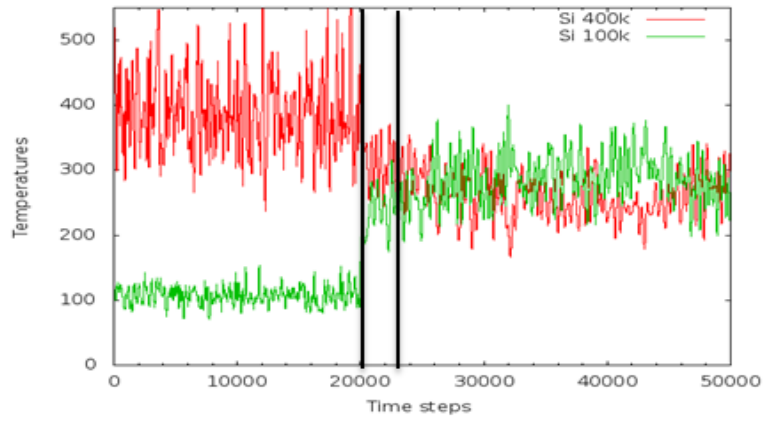
4.2.1.1 Silicon-Silicon-Layer Combinations

The silicon-silicon-layer at 400 K versus 100 K under different interfacial distance (closely contact, 1.0 / 2.0 times lattice constant of silicon) is modeled. Since the neighboring layers belong to the same material and the same kind of structure, the equilibration time from the removal point of the thermostats to the thermal equilibrium state is very short although such equilibration time duration renders a tendency of increasing with the increasing interfacial distance (Table 1).

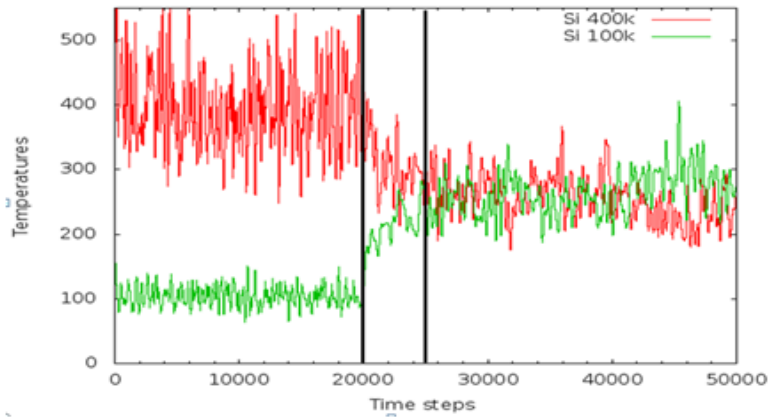
Table 1 Equilibration time for silicon-silicon-layer combinations under different interfacial distance

Interfacial Distance (\AA)	Time steps	Time (ps)
0.000	2,900	0.280
5.431	5,100	0.494
10.862	6,800	0.658

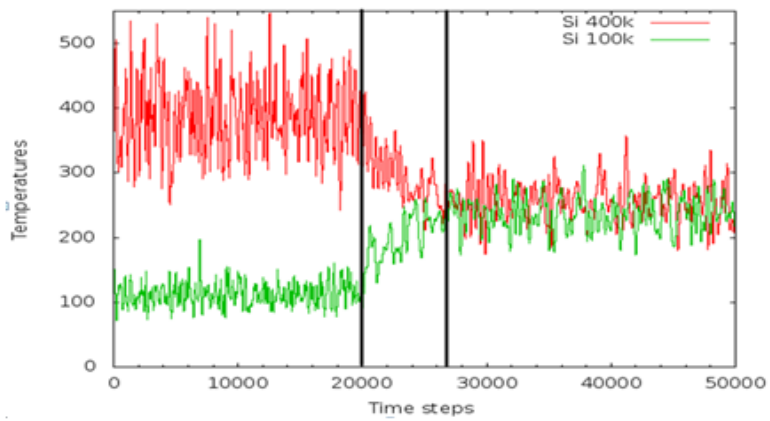
Simulation results show equilibration time of the case of closely contacted layers is the shortest, as seen in Fig. 8(a). The thermal transport phenomenon arising from these well matched layers attributes to heat conduction. Heat conduction within non-metallic solids occurs primarily by the propagation of elastic waves associating with the displacement of atoms from their lattice sites. Phonons are defined from these spatially localized, quantized units of propagating vibration waves. In semiconductors, like silicon, phonons are also the major energy carriers. Because the free electron density in a normal semiconductor is much lower than that in a metal, the participation of electrons can be neglected. For the layers established in our simulation, the length scale is approximate to lattice constant of silicon (2 atoms in the thickness direction), which is far less than the phonon mean free path (100 – 1000 \AA). Thus, the thermal transport mechanism is ballistic conduction. The vibrational energy of phonons transfers ballistically from one layer to another. In other words, the phonons keep along straight-line trajectories without destructions or redirections. Simulation result shows the equilibration time is about 0.2800 ps (Fig. 8(a)). Since the distance between the geometric centers of the neighboring silicon layers is set to be 5.431 \AA and the speed of sound of silicon is 5860 – 8480 m/s [15], the estimated time it takes for one way transport should be in the range of 0.0640 – 0.0927ps. Taking the back and forth thermal communication between



(a)



(b)



(c)

Fig. 7 Silicon-silicon-layer combination: (a) attached to each other, (b) interfacial distance: 1.0 lattice constant of silicon, (c) interfacial distance: 2.0 lattice constant of silicon

the contacting layers before the final thermal equilibrium state, the longer equilibration time of 0.2800 ps is reasonable in our simulation result.

When the two layers are separated and set with different interfacial distance, simulation results in Figs. 7(b) and 7(c) show that the equilibration time for the layers from the initial non-equilibrium to thermal equilibrium states gradually becomes longer as the interfacial distance increases (Table 1). The essential distinction between these latter cases (Figs. 7(b) and 7(c)) and the first case (Fig. 7(b)) is that the thermal energy transport transforms from the heat conduction to the thermal radiation with the enlargement of the layers interfacial gap. The dipole oscillation of the charges leads to the production of electromagnetic radiation. In the generated coupling electric and magnetic fields, radiating thermal energy emits from the body through its surface boundary. There are two modes for the electromagnetic radiation: far-field propagation electromagnetic modes and near-field evanescent mode that decays quickly over submicron length scales. In our simulated cases, the interfacial distance is at nanoscale, which is far less than the decay length of the near-field modes. Evanescent waves and phonon tunneling are responsible for the near-field energy transfer. The evanescent wave field of higher temperature layer excites the charges within lower temperature layer and dissipates its energy from high-temperature layer to low-temperature layer. In addition, the surface waves are hybrid modes that generate from coupling of electromagnetic field and mechanical oscillation of energy carriers inside the materials. For silicon whose energy carriers mainly composed with phonons, the hybrid mode is referred to as surface phonon-polariton. Due to the spatial difficulties of propagating waves caused by the enlargement of interfacial distance, equilibration time becomes correspondingly longer

due to weakened energy communication occurring on the surface of each layer. The simulation results are consistent with the theoretical analysis.

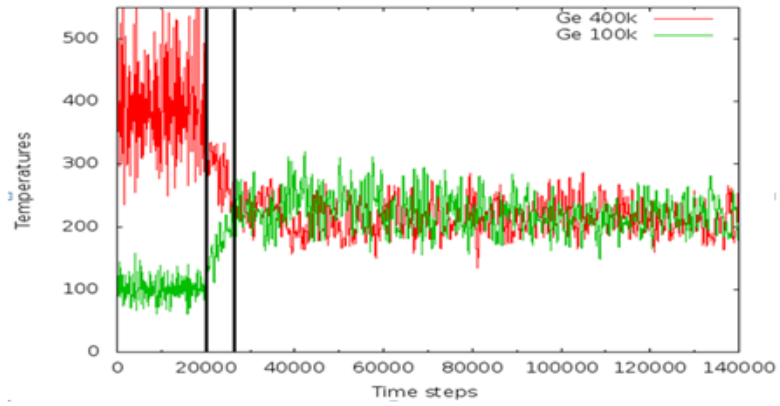
4.2.1.2 Germanium-Germanium-Layer Combinations

For the models of germanium-germanium-layer combinations, simulations are carried out under almost the same conditions as those in Section 4.2.1.1. Energy transport processes between two layers of germanium atoms at 400 K and 100 K under different interfacial distances are studied. The simulation results (Table 2) show longer equilibration time for both heat conduction and thermal radiation in the cases of germanium than that of the silicon.

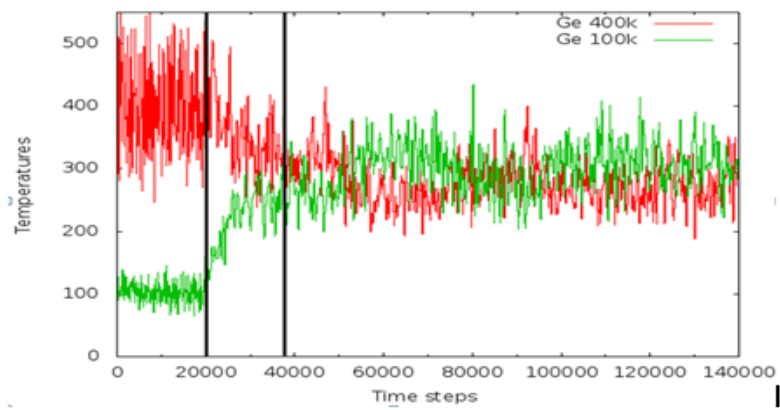
Table 2 Equilibration time for germanium-germanium-layer combinations under different interfacial distance

Interfacial Distance (Å)	Time steps	Time (ps)
0.000	6,500	0.629
5.658	18,000	1.742
11.316	20,000	1.936

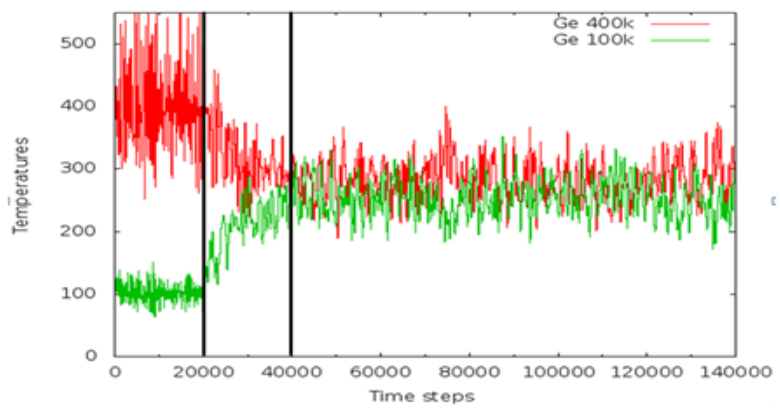
For the heat conduction (Fig. 8(a)), the longer equilibration time for germanium agrees with the macroscale property that germanium has a relatively lower thermal conductivity of $60.2 \text{ W} \cdot \text{m}^{-1} \cdot \text{K}^{-1}$ than that of $149 \text{ W} \cdot \text{m}^{-1} \cdot \text{K}^{-1}$ for silicon. As for the reason why equilibration time for thermal radiation (Figs. 8(b) and 8(c)) is also longer comparing with the cases in Section 4.2.1.1, we will have a more detailed explanation in Section 4.2.2.3.



(a)



(b)



(c)

Fig. 8 Germanium-germanium-layer combination: (a) attached to each other, (b) interfacial distance: 1.0 lattice constant of germanium, (c) interfacial distance: 2.0 lattice constant of germanium

4.2.2 Hybrid Materials Combinations

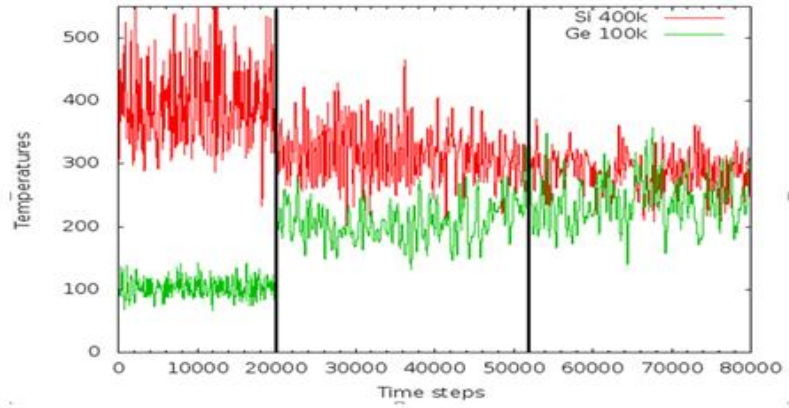
Each of silicon and germanium has four valence electrons. However, germanium will have more free electrons and more active thermoelectric characters than that of silicon under the same temperature, because germanium has lower band gap than that of silicon. On the other hand, the stability of silicon becomes one of the reasons that it is widely used in semiconductors at higher temperatures than germanium. To investigate the temperature and material dependence of both silicon and germanium, we carried out simulation of silicon-germanium-layer combinations at silicon (400 K) versus germanium (100 K) and silicon (100 K) versus germanium (400 K), respectively.

4.2.2.1 Silicon (400 K) versus Germanium (100 K)

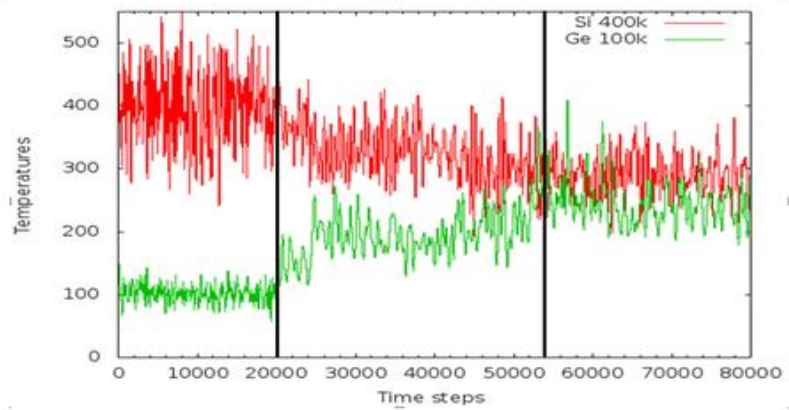
Since the temperature of silicon is set higher than that of germanium, the overall temperature evolution tendencies would be to cool down the silicon layers and to heat up the germanium. Figures 9(a)-(c) show the evolution of the temperatures of the silicon and germanium layers with different separation distances. Similar to the case of silicon-silicon-layer heat conduction (Fig. 7(a)), the silicon (400 K) - germanium (100 K) - layer combination (Fig. 9(a)) shows steep decrement and increment of temperatures during the process from non-equilibrium to dynamic thermal equilibrium. However, in the subsequent conduction process, temperatures of both the silicon and germanium layers tend very slow variation tendencies. It may be due to relatively small temperature difference between the two layers. The total equilibration time of thermal transfer is about 3.096 ps (32,000 time steps). But comparing the heat conduction process of the pure silicon-

silicon-layer combination (Fig. 7(a)) with the silicon (400 K) - germanium (100 K) - layer combination (Fig. 9(a)), one can conclude that the latter is distinctly longer.

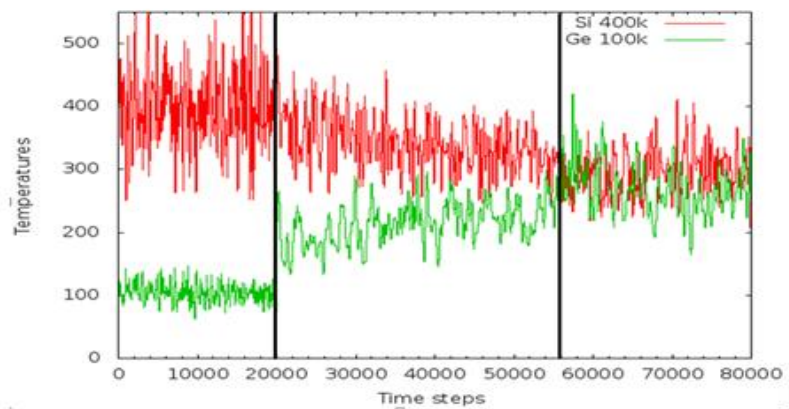
Probing from the atomic vibration point of view, the acoustic mismatch may be the main factor that leads to more difficult thermal communication for silicon-germanium-layer. In addition, mass difference is another factor that could contribute to the difference. When it comes to radiative heat transfer, simulation results (Figs. 9(b) and 9(c)) show that the slopes of both silicon and germanium temperatures become relatively gentle compared with the heat conduction case (Fig. 9(a)). Additionally, the equilibration time of thermal transfer for silicon (400 K) - germanium (100 K) - layer combination tends obviously much longer than that of the silicon-silicon-layer/germanium-germanium-layer combinations. Considering thermal radiation emission from the electro-dynamics point of view, the propagating and evanescent waves are emitted via the out-of-phase oscillations of charges of opposite signs. The couples of charges of opposite signs are named dipoles. The random fluctuation of charges in turn generates a fluctuating electromagnetic field, which is referred to as thermal radiation field. Because of the different kinds of thermal radiation field generated from the silicon and germanium layers, thermal communication difficulties in the inter-radiation field become dominant factors that lead to longer equilibration time in the silicon (400 K) - germanium (100 K) - layer combination than the pure material combinations. The larger interfacial distance is set up, the longer equilibration time needs for neighboring layers to reach thermal equilibrium. This is also consistent with the mechanism for results with gradually enlarged gaps in the silicon-silicon-layer combinations presented in Section 4.2.1.1.



(a)

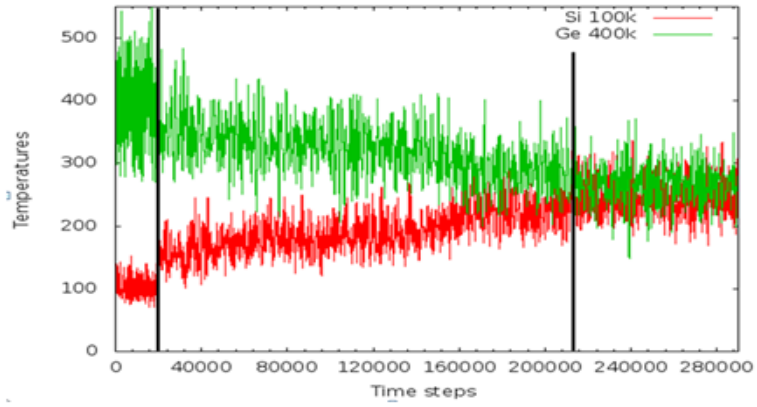


(b)

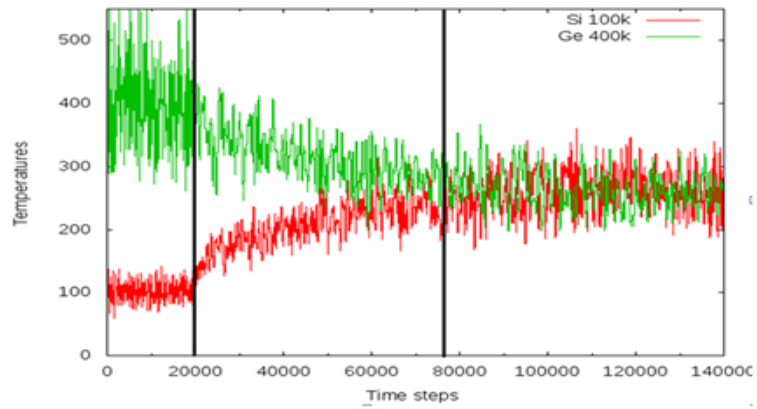


(c)

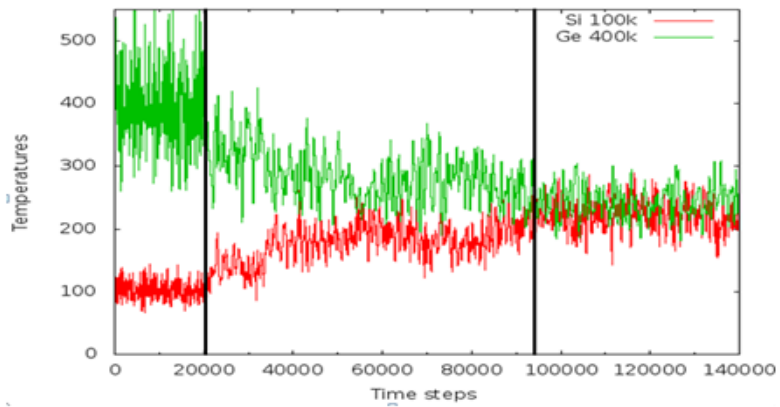
Fig. 9 Silicon-germanium-layer combination (400 K vs. 100 K) : (a) attached to each other, (b) interfacial distance: 1.0 lattice constant of germanium, (c) interfacial distance: 2.0 lattice constant of germanium



(a)



(b)



(c)

Fig. 10 Silicon-germanium-layer combination (100 K vs. 400 K) : (a) attached to each other, (b) interfacial distance: 1.0 lattice constant of germanium, (c) interfacial distance: 2.0 lattice constant of germanium

4.2.2.2 Silicon (100 K) versus Germanium (400 K)

We exchange the temperature configurations of the silicon layer and germanium layer to probe the impact of atoms' temperature difference during the thermal transport process. Like simulations performed before, in the silicon (400 K) - germanium (100 K) - layer combination model, we start our work from closely contacting layers.

The closely contacting layers thermal conduction case (Fig. 10(a)) and the gap enlarged layers thermal radiation cases (Figs. 10(b) and 10(c)) render much longer equilibration time than those at the same conditions of silicon (400 K) - germanium (100 K) - layer cases (Figs. 9(a)-(c)). It shows that the thermophysical properties of nanocomposite materials depend on not only the properties of their individual constituents but also their morphological and interfacial characteristics. The heat conduction results (See Figs. 9(a) and 10(a)) indicate that the thermal contact conductance in the interface is significantly affected by how the temperatures differences are imposed. As shown in our simulation results for heat conduction (Figs. 9(a) and 10(a)), it is easier for the thermal energy transfer from the silicon side to the germanium side under the condition of relatively lower temperature for germanium layer. Thus, the ballistic thermal conductance becomes lower when the temperature for germanium is higher than that of silicon. In addition, the heterogeneous effect is another factor deserving our attention. For the case of silicon (100 K) - germanium (400 K) - layer combination, the acoustic mismatch accounting for long-wavelength phonons is the main impedance in the interfacial thermal conduction. From the phonon density of states point of view, the diffusion of scattering phonons

mismatch is another factor that weakens the thermal transport for silicon and germanium combinations than that of the pure material combinations.

The thermal radiation results for silicon (100 K) - germanium (400 K) - layer combination demonstrated a phenomenon: when the interfacial distance between silicon and germanium layers increases, the corresponding equilibration time to reach thermal equilibrium becomes much longer than that of the same cases for the silicon (400 K) - germanium (100 K) - layer combinations (See Tables 3 and 4 for details).

Table 3 Equilibration time for silicon (400 K) - germanium (100 K) - layer combinations under different interfacial distance

Interfacial Distance (Å)	Time steps	Time (ps)
0.000	32,000	3.096
5.658	34,000	3.289
11.316	36,000	3.483

Table 4 Equilibration time for silicon (100 K) - germanium (400 K) - layer combinations under different interfacial distance

Interfacial Distance (Å)	Time steps	Time (ps)
0.000	194,000	18.770
5.658	57,000	5.515
11.316	74,000	7.160

As explained before, different kinds of evanescent waves are generated in the surfaces of silicon and germanium, respectively. Because of the interfacial distances are in the sub-nanometer and nanometer in our simulated cases, which are far less than the decay length of the near field mode, the vacuum gap between neighboring layers can be treated as space filled with evanescent waves along the boundaries of both facing layers.

4.2.2.3 Further Discussion on Equilibrium Time

In our simulated models, the characteristic structural length is much shorter than the photon wavelength. Thus, the wave properties of the radiation energy should be considered. Because of the quantum and vacuum fluctuations of atoms and electrons, there will be a fluctuating electro-dynamical field inside the layers. In addition, according to the boundary conditions of macroscopic electro-dynamics, a continuous electric and magnetic field has to exist in the spatial gap. That is to say, there is also a fluctuating electromagnetic field outside the layers produced by the fluctuating internal source. The difference of equilibration time can be explained by the total internal reflection. The index of refraction of germanium is greater than that of silicon, and both of them are greater than 1 in vacuum [80]. Analyzing from the wave emission point of view for the higher temperature layer of germanium, let us describe the wave incident from germanium to vacuum as the electric field $E_{Ge \rightarrow vacuum} e^{i(k_{Ge}r - \omega t)}$, where k_{Ge} denotes the wave vector from germanium to vacuum. To simplify the three-dimension thermal radiation field, let us assume that the waves are travelling in the $x - y$ plane only, as seen in Fig. 11.

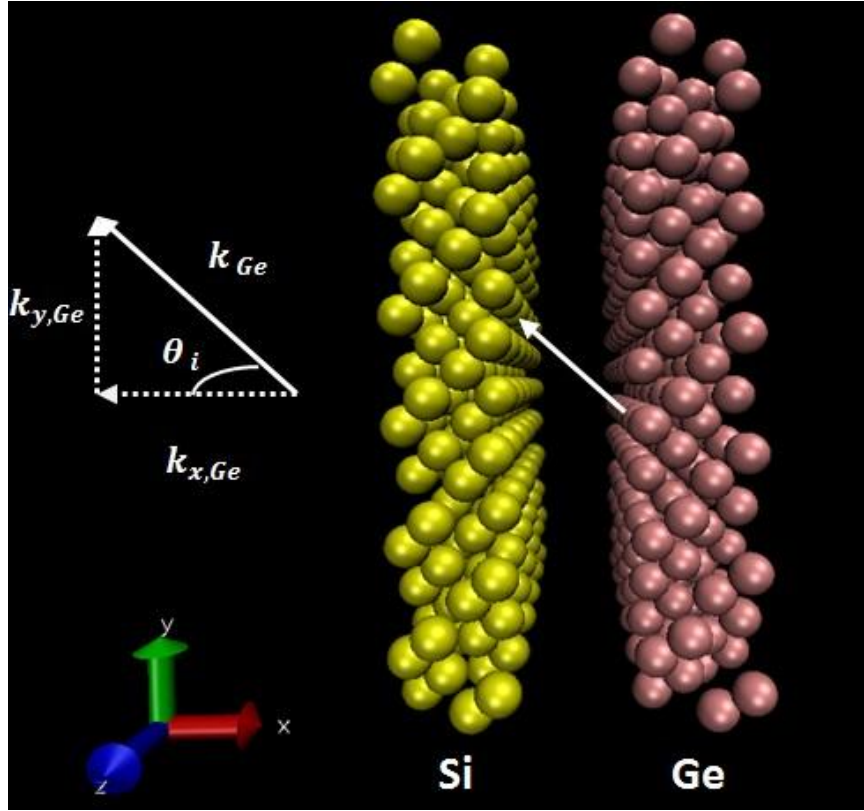


Fig. 11 Periodic display of the silicon-germanium-layer combination in y - and z -direction (the interfacial distance equals the lattice constant of germanium)

The amplitude of the wave vector $k_{Ge \rightarrow vacuum} = |\mathbf{k}_{Ge \rightarrow vacuum}|$ equals to $n_{Ge}k_0$, where k_0 is the magnitude of the wave vector in vacuum.

Thus, the x -component of the wave vector in the surface of germanium layer is:

$$k_{x,Ge} = \sqrt{k_0^2 - k_{y,Ge}^2} \quad (40)$$

The y -component of the wave vector can be expressed in term of the angle of incidence:

$$k_{y,Ge} = n_{Ge}k_0 \cdot \sin\theta_{i,Ge} \quad (41)$$

where θ_i is the angle of incidence. Since the index of refraction of germanium is greater than 1, there will be an angle of incidence that makes the entire energy irradiating into the vacuum gap be reflected back to the germanium layer. Thus, a critical angle (θ_c) at which the angle of incidence is equal to the angle for total internal reflection can be defined. At the moment the y-component of the wave vector is:

$$k_{y,Ge} = k_0 \quad (42)$$

We can derivate $\theta_{c,Ge}$ as

$$\theta_{c,Ge} = \sin^{-1} \frac{1}{n_{Ge}} \quad (43)$$

In our simulated system, periodic boundary condition is employed in three dimensions. Hence, the y-component of the vector is conserved because the layers are infinite along the y-direction. Similarly, the x-component of the wave vector generated from silicon to germanium can be expressed as

$$k_{x,Si} = \sqrt{k_0^2 - k_{y,Si}^2} \quad (44)$$

and the critical angle of incidence is

$$\theta_{c,Si} = \sin^{-1} \frac{1}{n_{Si}} \quad (45)$$

Thus, we can conclude that $\theta_{c,Si} > \theta_{c,Ge}$ (Fig. 12).

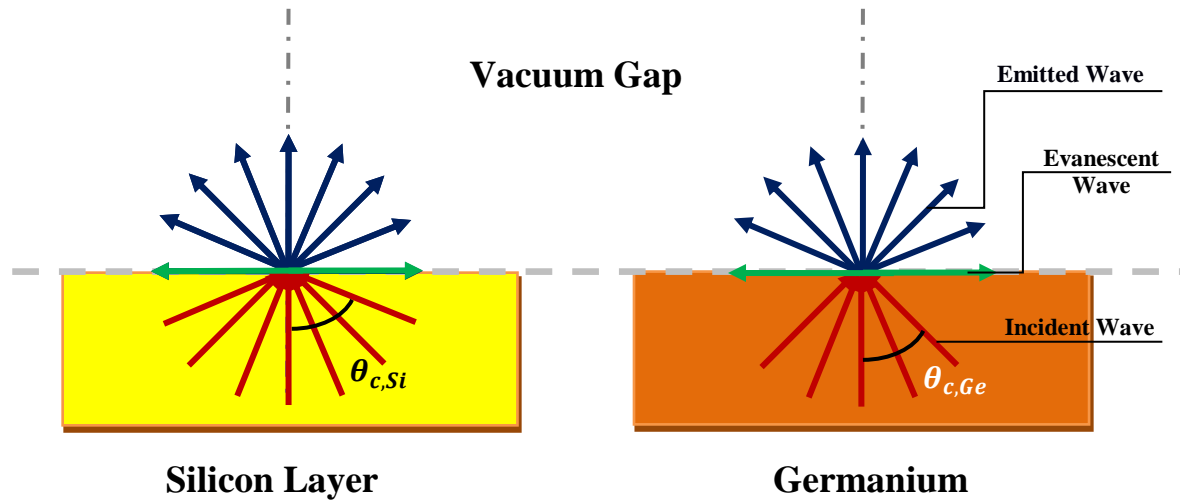


Fig. 12 Schematic show of the incident waves, emitted waves, evanescent waves during the electromagnetic waves emission process

The incident waves, sourcing from germanium and silicon layers, have the same probabilities involved in all direction ($0^\circ - 180^\circ$). The percentage of incident waves that can be effectively transformed as evanescent waves on the surface of germanium layer will be less than that on the silicon layer, due to the relatively greater refraction number of germanium.

Reversely, peering from the scope of energy absorption, the direction is from the vacuum to silicon/germanium layers. Here, the angle of incidence ranges from 0° to 90° , which means that various incident waves can directly penetrate into the silicon/germanium layers. Furthermore, since there are more electrons circling around the germanium nuclei than that of silicon nuclei, even if the same amount of thermal energy penetrate into the two materials, it would be much easier for the germanium layer to absorb the external

energy and convert it into internal energy. In other words, the temperature increasing rate for germanium (100 K) layer would be faster than silicon (100 K) layer.

Therefore, from both the energy emission and absorption point of view, owing to dual action of evanescent wave emission and absorption capability, the heat transfer rate for the silicon (400 K) - germanium (100 K) - layer combinations is greater than silicon (100 K) - germanium (400 K) - layer combinations in our simulation results, which shows an agreement between the simulation results with the theoretical analysis.

As for the reason why the equilibration time for the gap of 11.316 \AA is longer than that of the gap of 5.658 \AA cases in both the silicon (400 K) - germanium (100 K) - layer combination and the silicon (100 K) - germanium (400 K) - layer combination, we can interpret it with the evanescent-wave coupling [81]. As aforementioned, the evanescent waves are generated on both the silicon and germanium layer surfaces. The sort of electromagnetic waves decay exponentially in electromagnetic field. The coupling phenomenon occurs by placing two electromagnetic fields close together so that the evanescent field generated by one layer does not decay much before it reaches to the neighboring layer. Thus, for larger interfacial distance set up in the simulated model, the less coupling waves are involved in the vacuum gap. Consequently, the thermal energy transport efficiency will be lower for larger interfacial gap.

Chapter 5 Femtosecond Laser Processing of Germanium:

An Ab Initio Molecular Dynamics Study

5.1 Modeling and Simulation

The ab initio molecular dynamics simulation was started with germanium crystal at room temperature (300 K). The CPMD package 3.15.3 [65] based on plane wave pseudopotential implementation of FT-DFT and incorporating self-consistently the effects of thermal electronic excitations and fractionally occupied states was used. As introduced in Section 2.1, certain method is particularly congruent to deal with the electronically hot problems. A cubic system containing 64 germanium atoms were modeled within 11.316 \AA at x -, y - and z - directions, which corresponds to the density of germanium at 5.323 g/cm^{-3} . The Γ point was used to sample the Brillouin zone of the molecular dynamics supercell. The simulation time step was set 4 a.u. ($\sim 0.096,755\text{ fs}$) to obtain integration of the ionic degrees of freedom. The exchange correlation in our simulation was represented by the local density approximation (LDA) [82]. We adopted the norm conserving pseudopotentials with Stumpf-Gonze-Scheffler [79] pseudolization method [83]. Periodic boundary conditions were applied in all three directions of the primitive cell of diamond cubic crystal structure. In our simulation, all cases adopted the cutoff of 35 Ry to expand the electronic orbitals in plane waves. The single particle electronic states were set as 200 to take all the levels of electronic excitation into consideration.

In order to perform FT-DFT simulation, the wavefunction optimization and geometric optimization were performed first to calculate the electronic structure of the system and the optimization results showed the cutoff of 35 *Ry* is sufficient enough to get the converged energies. After obtaining the optimized electronic structure, all the cases were run for 1,000 time steps at room temperature (300 *K*) with Nose Hoover [72] thermostats imposed on each degree of freedom for both electrons and nuclei, so that the electronic subsystem and ionic subsystem could reach to sufficient equilibrium state before laser irradiation.

In our simulation, due to the fact that the estimated relaxation time for the electron-electron interaction (~ 10 *fs*) is much shorter than the electron-ion interaction (~ 1 *ps*) and ion-ion interaction (~ 10 *ps*), the electrons subsystem was assumed to achieve high level temperature instantaneously, during the period was less than 1 *ps* since laser irradiation. However, the ionic subsystem was treated tardily respond to the irradiation and let it run freely to reach final equilibrium with the electronic subsystem. We can find the same kinds of approximation and simulation approach simulating the scenario of femtosecond laser irradiation, which uses the constant electron temperature control to characterize the instantly excited electronic subsystem. Two typical treatments adopting the aforementioned methodology are laser melting of silicon [36] for 0.4 *fs* and graphite [53] for 0.5 *fs*. Besides using the free energy functional approach, simulation technique of elevating electron temperature as a constant value to represent the excited electronic subsystem, can also be seen in the investigation of crystal stability in the density functional perturbation theory calculations [35] and ab initio molecular dynamics simulation of femtosecond laser interaction with vitreous silica [84]. In addition, as

reported in the estimations of experiments, the electron temperature can be as high as 100,000 K [53]. Therefore, we carried out simulation of femtosecond laser irradiation by instantly increasing the electron temperature to 20,000 K, 25,000K, 30,000K, 35,000K, 40,000K , 50,000K and 60,000K from the 1,001th to 2,000th time steps, which corresponded to the time duration of ~ 100 fs. In order to observe the further results of femtosecond laser processing of germanium, we carried on the simulation with constant total energy lasting for another 2,000 time steps by removing the energy control of electronic subsystem.

The evaluation of electron temperature was based on the Maxwell-Boltzmann distribution of electron gas

$$\langle E \rangle = \frac{3k_B}{2} \langle T \rangle \quad (46)$$

Therefore, the conversion of electron temperature at 1K in terms of the energy of $8.6173 \times 10^{-5} eV$ is used in the thermostats for temperature control. From the engineering prospective, when it refers femtosecond laser material processing, laser pulse duration and laser fluence (intensity) are two crucial parameters to characterize femtosecond laser. In this study, the instant incident of laser fluence can be expressed by the energy increment of electron subsystem.

$$J = \frac{N_e N_I c \Delta T}{d_x d_y} \quad (47)$$

where N_I and N_e refer to the number of atoms included in the system and the number of electrons circling around one germanium nuclei; c is the conversion coefficient from

electron temperature to average electron energy; ΔT is the electron temperature increase induced by laser irradiation; and d_x , d_y are the width and length of the modeled system. The calculated average electron energy, laser fluence and laser intensity is listed in Table 5.

Table 5 Femtosecond Laser Parameters in the Simulation

Computational Case	Electron Temperature (K)	Average Electron Energy (eV)	Femtosecond Laser Fluence (J/cm^2)	Femtosecond Laser Intensity ($10^{12} W/cm^2$)
1	20000	1.7235	0.0434	0.4490
2	25000	2.1543	0.0545	0.5630
3	30000	2.5852	0.0655	0.6769
4	35000	3.0161	0.0765	0.7908
5	40000	3.4469	0.0875	0.9048
6	50000	4.3086	0.1096	1.1328
7	60000	5.1704	0.1316	1.3607

5.2 Results and Discussion

5.2.1 Temperature Evolutions

We calculated the temperatures of the ionic subsystems along with the MD simulation for all the cases. As is shown in Fig. 1, the phase change of melting and evaporation occurred around the electron temperature conditions of 25,000 K and 50,000 K. We calculated the temperature of ions according the following definition

$$T_I = \frac{2\bar{E}_I}{3(N-1)k_B} \quad (48)$$

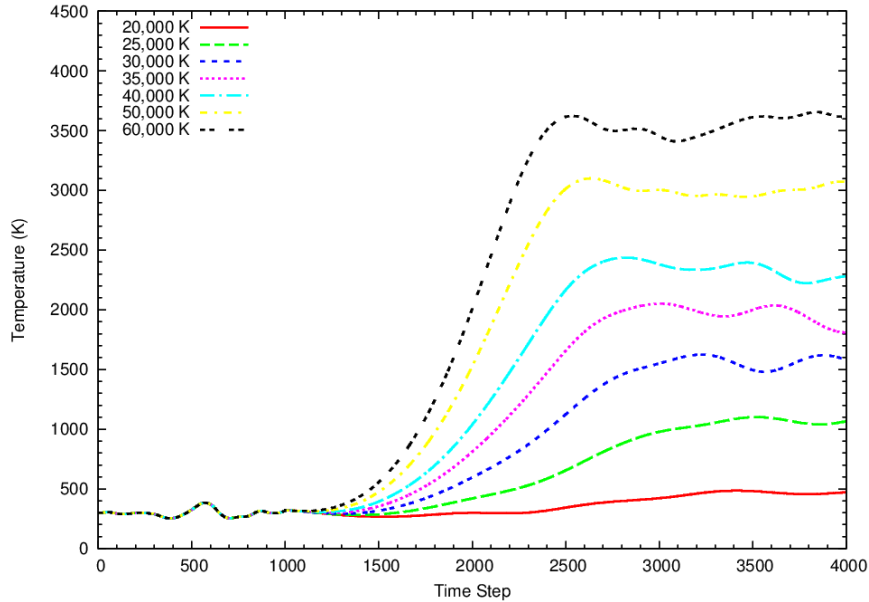


Fig. 13 Ionic temperatures

As what can see from Fig. 13, the lattices remain at relatively lower temperatures in the first 1,000 time steps of laser irradiation. When the condition of femtosecond laser interaction is imposed, the relatively low temperature states of ions keep about 200 time steps ($\sim 0.2 fs$) and then are followed by slow temperature increments from 1,200 to

1,500 time steps. After 1,500 time steps, the ion temperatures show abrupt increases, especially for cases of the electronic subsystems with relatively higher energies. The advents of ion temperatures exceeding the melting and boiling points are also early for the electron systems with higher temperatures than those with lower electron temperatures. After the temperatures of ion subsystems increasing to certain values, they stayed and oscillated in small ranges at temporarily equilibrium states with the electron subsystems. The temperature curve (1,000 – 4,000 time steps) for the case of 20,000 K is distinctly different from that of 25,000 K, which indicates that for the case of 20,000 K femtosecond laser almost cannot make the ions to break most of the valence bonds connecting them but only keep with wild oscillations around their equilibrium positions. The same condition of femtosecond laser distinct threshold of $0.15 J/cm^2$ that enables the strong excitation and nonthermal process was experimentally measured for femtosecond processing of gallium arsenide [85]. It is not definite to draw the final conclusion that the ions will still keep at low temperatures for the case of electron temperature 20,000 K, with the time duration to picosecond time scale. As pointed in Lindemann's law [86], once the vibrational amplitude reaches up to 10% of the nearest neighbor distance, the vibration will disrupt the equilibrium crystal lattice and the melting phenomenon eventually takes place. The short simulation period could not reveal the melting phenomena for this case. Nevertheless, we can find that even though the simulation process lasts for $\sim 0.3 ps$, the temperature evolutions for the seven cases still distinguish from each other and the ion temperatures are much lower than the corresponding electron temperatures for all the cases. The phenomena can be interpreted from two aspects. On one hand, the incident energy heats the electrons more strongly

than the ions. On the other hand, atoms and ions are much heavier than electrons, which lead to the inefficient thermal energy transfer in a two-body collision because the masses are dissimilar. Moreover, as computed in Table 5, the laser fluence exciting electron temperature to 60,000 K is $0.1316 J/cm^2$, which is in the same order of magnitude as reported for the femtosecond laser ablation threshold fluence ($0.2 J/cm^2$) for silicon [87].

5.2.2 The Free Energy Calculation

The quantities of free energies of the simulation systems were recorded to get a further insight of the changes of the microsystem. The Fermi-Dirac distribution was used for the purpose of filling the electronic states as a function of the temperature in the free energy functional calculation.

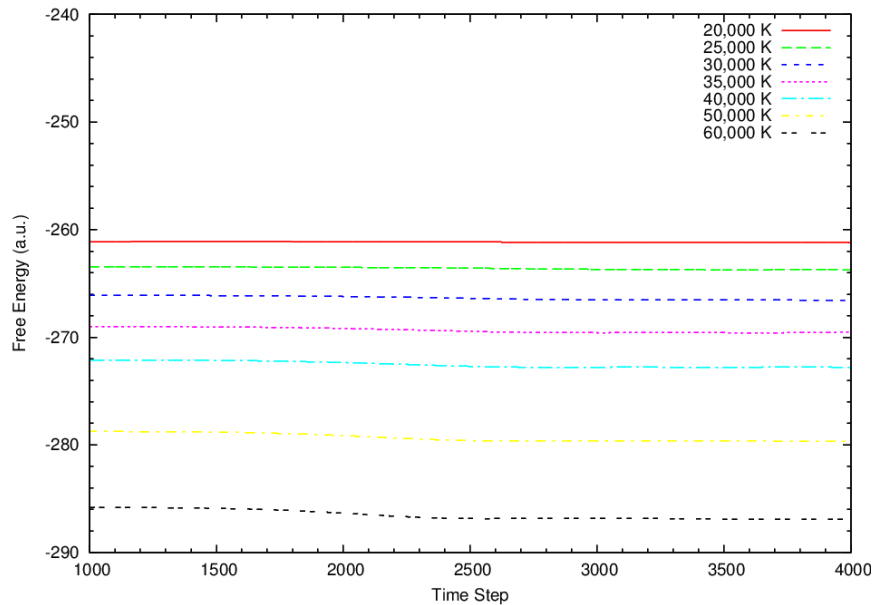


Fig. 14 Free energies for all the cases

Figure 14 shows the free energies of the system under different femtosecond laser irradiations. With the increasing laser energy intensities, the free energy drops greater ranges and stays at lower energy values. To get the results more explicitly, the detailed evolution curves of each case are shown in Figs. 15(a)-(g). The curves for free energies correspond to the ion temperature profiles shown in Fig. 1. It means that while there is a free energy drop (see Fig. 15), there is an increment of the ion temperature (see Fig. 13). This kind of trends can also be found in the simulation result of silicon [88]. The comparisons among Figs. 15(a)-(g) demonstrate that even though the electron temperatures induced by the incident laser are tens to hundreds times higher than the ion temperature, the electronic-ionic energy exchange cannot happen instantaneously and efficiently for some cases that the electron temperatures lower than a criteria (see the 20,000 *K* and 25,000 *K* cases).

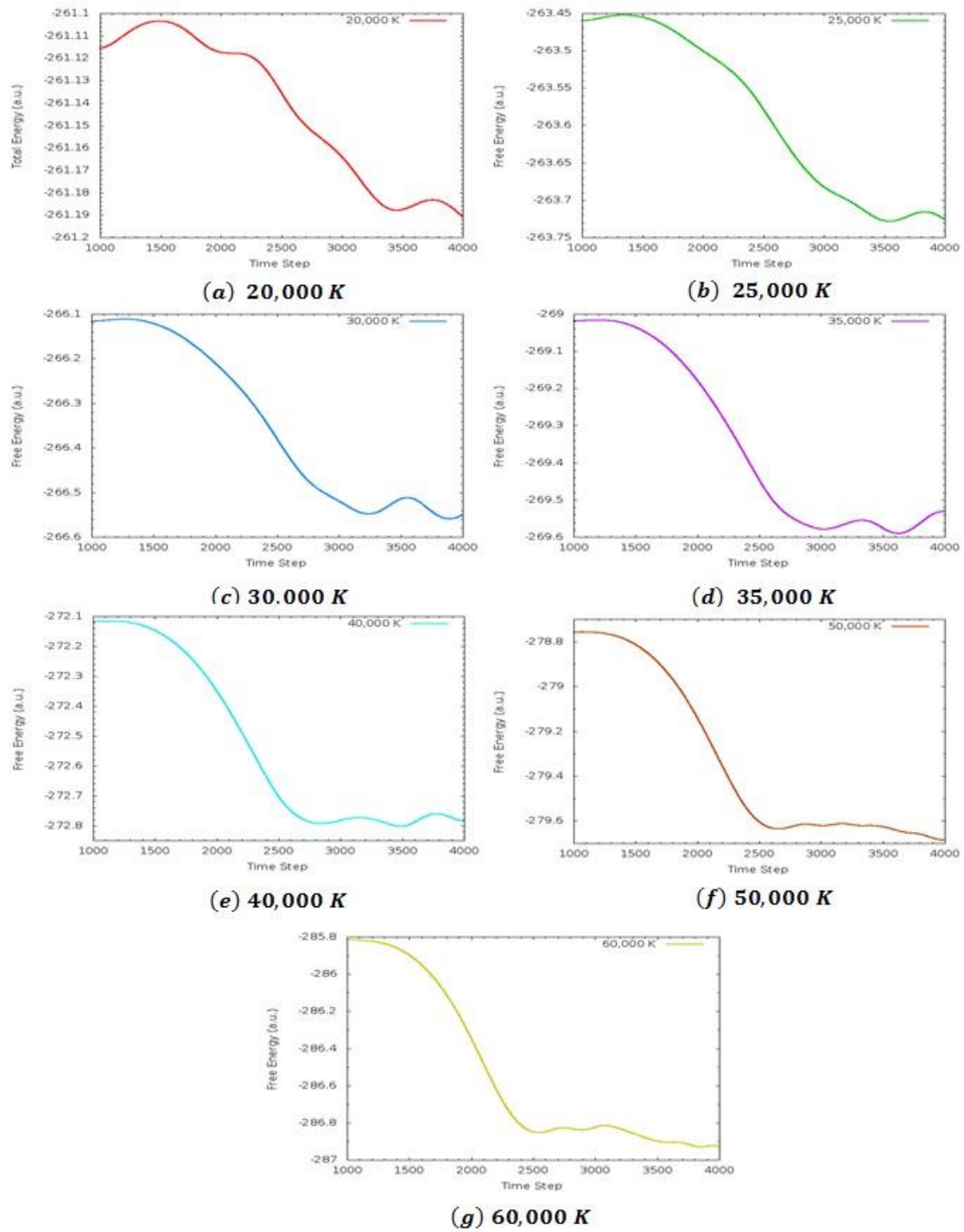


Fig. 15 Free energy change for different cases

5.2.3 Nanostructure Changes due to Thermal Melting and Evaporation

To understand the melting effect of femtosecond laser nanolithography, the nanostructure change is the primary parameter to evaluate the results of irradiated germanium. The radial distribution function (RDF) $g(r)$ describes how the density varies as a function of distance from a reference particle. It is also referred to as pair distribution function or pair correlation function, which describes how, on average, the atoms in a system are radially packed around each other. As an important structural characteristic of crystal germanium, we computed RDF based on the trajectories of atoms produced at different simulation stages from the initial equilibrium state at room temperature to the subsequent laser irradiation process. In our RDF calculations, we set the ionic radii as 0.67 \AA for germanium, respectively. In each case, we took the number of δr steps as 1,000. From the calculated RDF, the probability to find an atom in a shell dr at the distance r of another atom chosen as a reference point can be obtained. Mathematical expression of the RDF is

$$g(r) = \frac{Ndn(r)}{V_{vol}4\pi r^2 dr} \quad (49)$$

where $dn(r)$ represents the number of atoms inside a shell region between r and $r + dr$ for a given system. N and V_{vol} are the total number of atoms in the model and its volume, respectively. Another reason that we calculated the RDF is that the internal energy of the system is related to the pair correlation function.

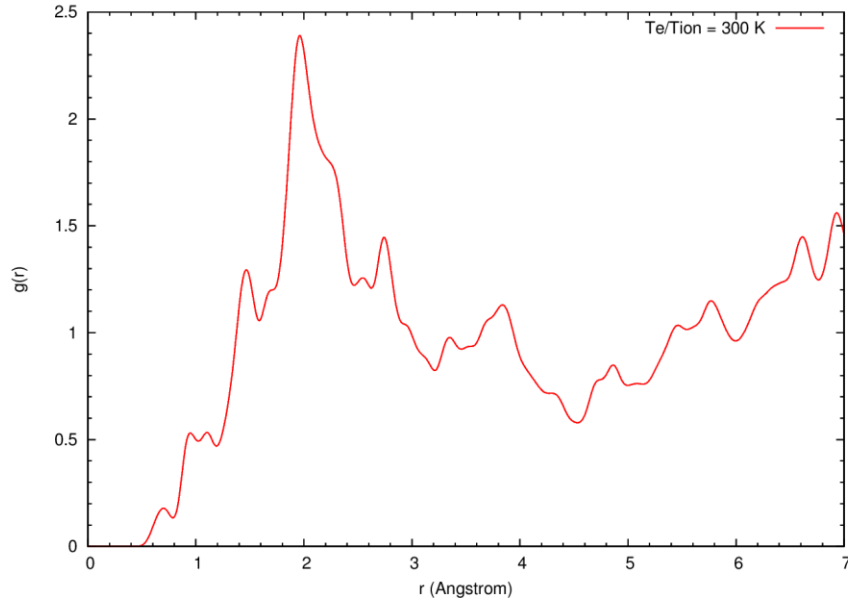


Fig. 16 RDF of germanium crystal at room temperature (300 K)

The RDFs for the room temperature were calculated first and the results are shown in Fig. 16. It can be seen that there are one peak and one valley, which reflect the regular arrangement of germanium atoms in the crystal at room temperature. In order to obtain the information of solid, liquid and gas phases, we chose the cases with electron temperatures of 20,000 K, 30,000K and 60,000 K to calculate the RDFs for comparison (see Figs. 18-20). The temporarily stable ion temperatures for the three cases are approximately 400K, 1,600 K and 3,400 K, respectively. We also computed the RDFs for germanium in three phases (corresponding to 400K, 1,600 K and 3,400 K) that the electron temperature and ion temperature are the equal (see the purple curves in Figs. 17-19). The maximum distance in real space to sample the number of germanium atoms was chosen to be 7 Å. Due to the abrupt shock of high level energy in the electronic subsystem, the nanostructure of germanium is disturbed since the initial irradiation stage of femtosecond laser. The emergences of curves in low atomic range indicate the

germanium atoms are ionized. However, the RDFs in Figs. 17-19 show the maximum peaks occur at different time stages. Namely, the case of electron temperature 20,000 K during 1,001 – 2,000 time steps (see red curve in Fig. 17), the case of electron temperature 30,000 K during 2,001 – 3,000 time steps (see green curve in Fig. 18), the case of electron temperature 60,000 K during 3,001 – 4,000 time steps (see blue curve in Fig. 19). Because the RDFs in Figs 17-19 represent distinctly differently phase states, the shapes and values correspondingly distinguish from each other. The differences of occurrences for the three cases reveal the atomic distances are separated due to the shock of incident lasers. With the higher intensity, the larger separation occurs (see the valleys in the red curves in Fig. 18 and Fig. 19). Subsequently, the random collisions of atoms happen. But due to the separation, the maximum peak that shows the greatest probability of finding atoms at short distance ($0-1\text{\AA}$) is consequently later.

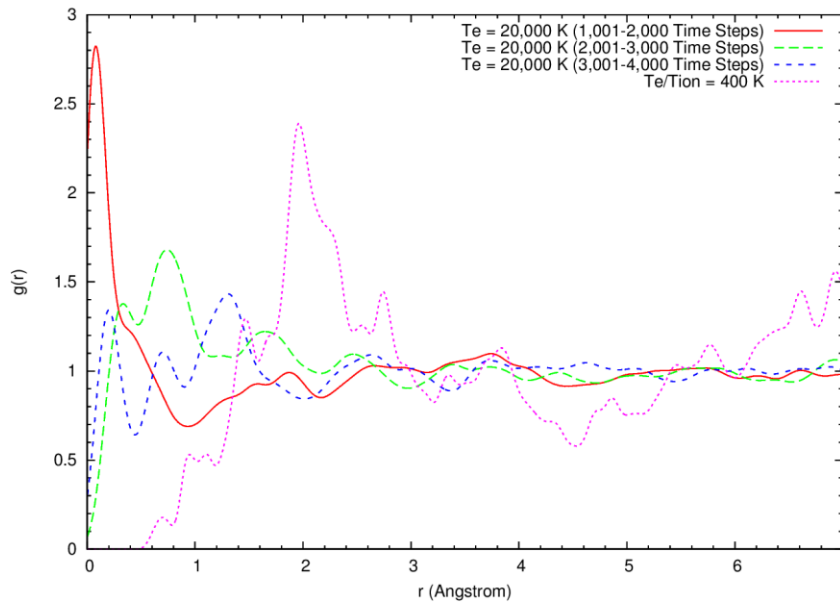


Fig. 17 RDFs at different stages, solid state (20,000 K)

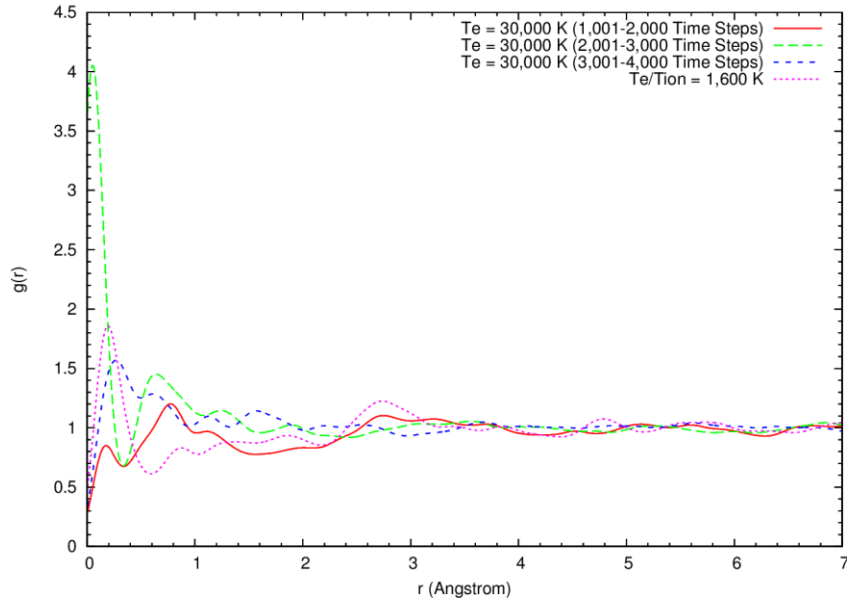


Fig. 18 RDFs at different stages, liquid state (30,000 K)

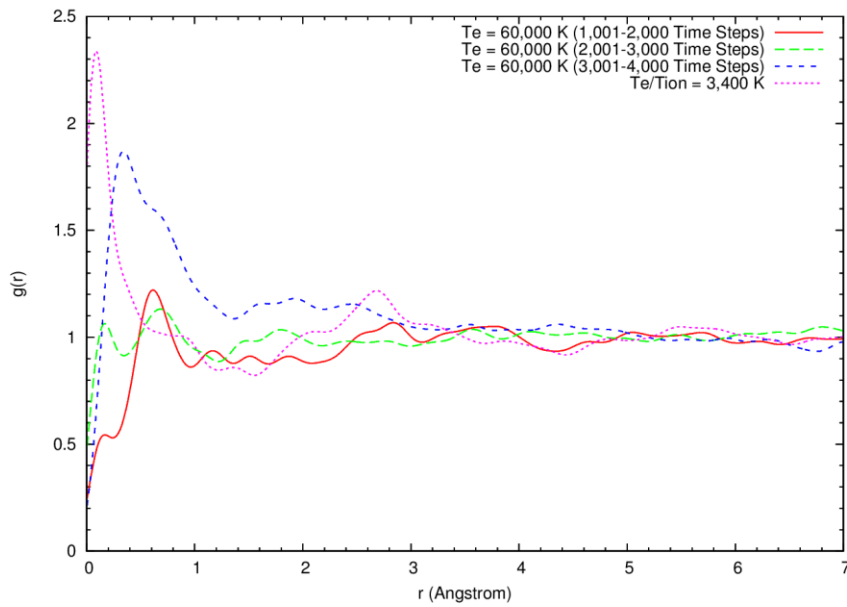


Fig. 19 RDFs at different stages, gas phase (60,000 K)

For the case of electron temperature 20,000 K, the comparisons between the purple curve and the blue curve, even though the ion temperatures are approximately equal, the RDF results show the completely different profiles. We can see that even though the crystal is not melted by the hot

electrons, the nanostructure has already changed. As seen in Fig. 13, the temporarily stable temperature of the case of 20,000 K is around 400K. Thus, to make the prediction even more persuasive, we calculated the RDF of germanium, whose temperatures of electronic subsystem and the ionic subsystem are both set as 400 K (see the purple curve in Fig. 17). The profile of the purple curve ($T_{e&I} = 400$ K) in Fig. 17 resembles the curve ($T_{e&I} = 300$ K) in Fig. 16, which indicates atoms in the solid germanium are kept as ordered arrangements.

5.2.4 Thermal Motion of Atoms

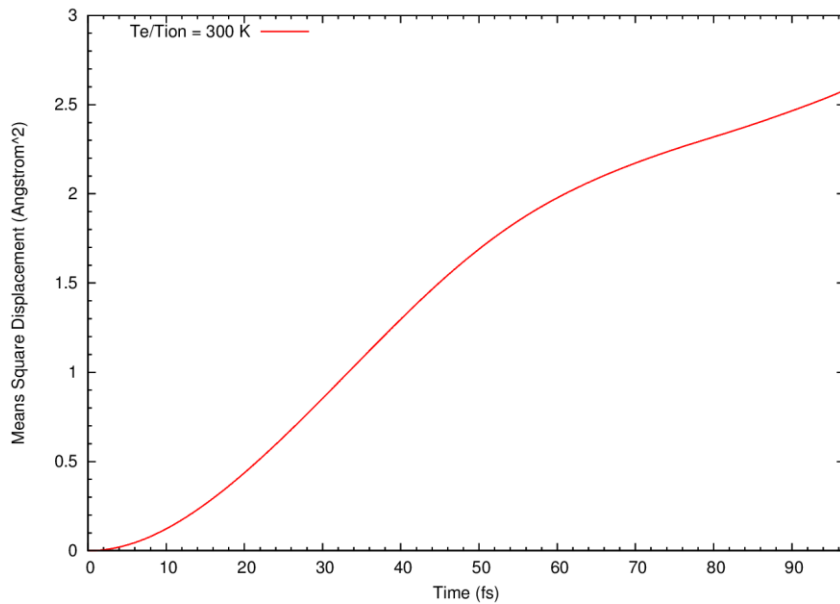


Fig. 20 MSD of germanium crystal at room temperature (300 K)

To quantitatively measure the extent of spatial random motion of the atoms, we calculated the mean square displacement (MSD) of the atomic thermal motion for germanium at different phases with selected stages like section 5.2.3. In physics, the trajectories caused by random collisions of atoms from each other are very complex

during the evolution of a MD simulation process. By adding the square of the distances, the MSD method conquers the drawback of elimination effects induced by the addition of the positive and negative values counting from a prefixed position. The MSD is mathematically defined by taking the average of the summations of square distance. It can be expressed

$$MSD(t) = \langle r^2(t) \rangle = \langle |\mathbf{r}_i(t) - \mathbf{r}_i(0)|^2 \rangle \quad (50)$$

where $\mathbf{r}_i(t)$ represents the position of the atom i at the time t and $\langle \dots \rangle$ is denoted as an average on the time steps and the particles.

Figure 20 shows the calculated MSD of the solid state germanium and the value at the end of the 1,000 time steps (96.755 fs) is about 0.7 \AA^2 . Because the thermal motion of atoms is only characterized by phonon vibrations, there are no appreciable MSD. In Figs. 21-23, the calculated MSDs of different simulation stages since the femtosecond laser irradiation are plotted. A general tendency of increasing values at the ending point of each 1,000 time steps is revealed in Figs. 21-23. In addition, for the cases of higher electron temperature, the MSD amplitudes are correspondingly higher. The discrepancies of purple curves between the other three curves verify the predication that germanium with equal electron temperature and ion temperature is different from the ones that the electrons are excited. Moreover, the slope of red curve in Fig. 21 is relatively steeper than the purple curve in Fig 21. Thus, we can see that the motion property of the laser irradiated germanium is more like fluids rather than the germanium with same temperature at the solid state. The remarkably high energy femtosecond laser irradiated MSD is also reported for vitreous silica [84], whose ion temperature is $\sim 500 \text{ K}$ after

irradiation. The other point that deserves our attention is the red curves in each of Figs. 21-23, when they are compared with the green and blue curves. We can find that in Fig. 21, the final value of red curve MSD is 7.5 Bohr^2 . However, the squared distance of thermal motion of the green one in Fig. 21 is more than 1.47 times of that in red. In addition, the ratio of the final value between blue curve and green curve gradually narrow down from Fig. 21 to 23.

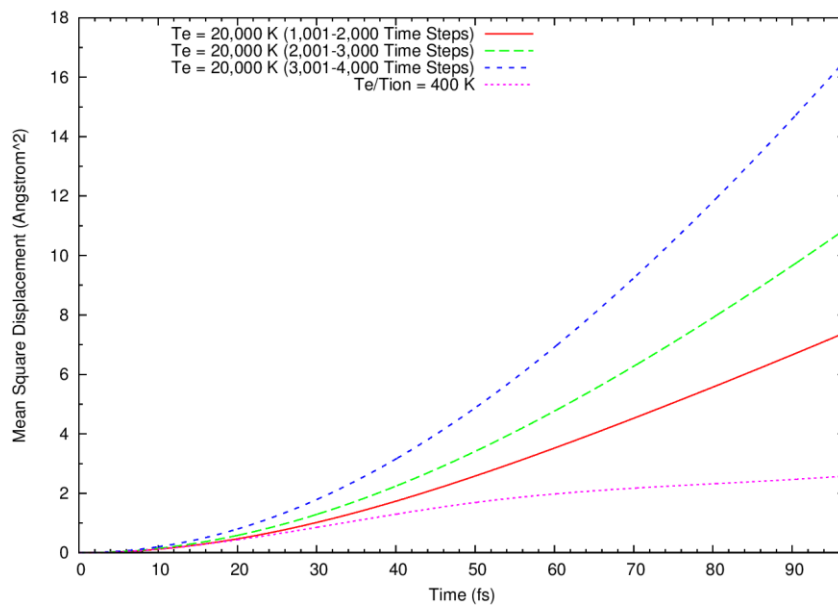


Fig. 21 MSDs at different stages, solid state (20,000 K)

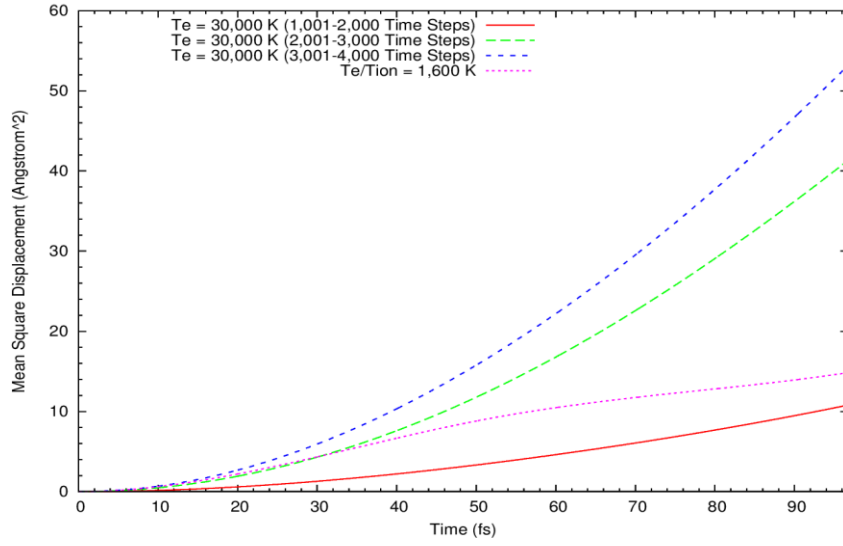


Fig. 22 MSDs at different stages, liquid state (30,000 K)

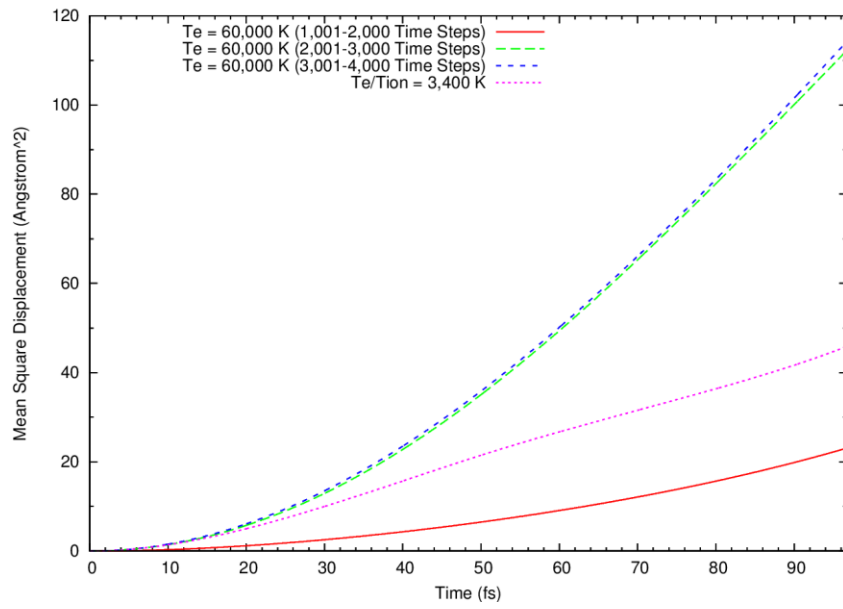


Fig. 23 MSDs at different stages, gas state (60,000 K)

5.2.5 Dynamical Property of Velocity Autocorrelation Function

The velocity autocorrelation function (VAF) is also an important parameter to characterize the dynamical properties of femtosecond irradiated germanium. It is important in revealing the underlying nature of the dynamical process operating in the simulated molecular system. The velocity autocorrelation is mathematically written as:

$$Z(t) = \frac{\sum_{i=1}^N (\mathbf{V}_i(t) \cdot \mathbf{V}_i(0))}{\sum_{i=1}^N (\mathbf{V}_i(0) \cdot \mathbf{V}_i(0))} \quad (51)$$

where $\mathbf{V}_i(t)$ includes the three components of the velocity $v_x(t)$, $v_y(t)$ and $v_z(t)$. We computed the VAFs for system with electronic temperature at 300 K, 20,000 K, 30,000 K and 60,000 K, respectively. The sampling time period is 1,000 time steps for all cases.

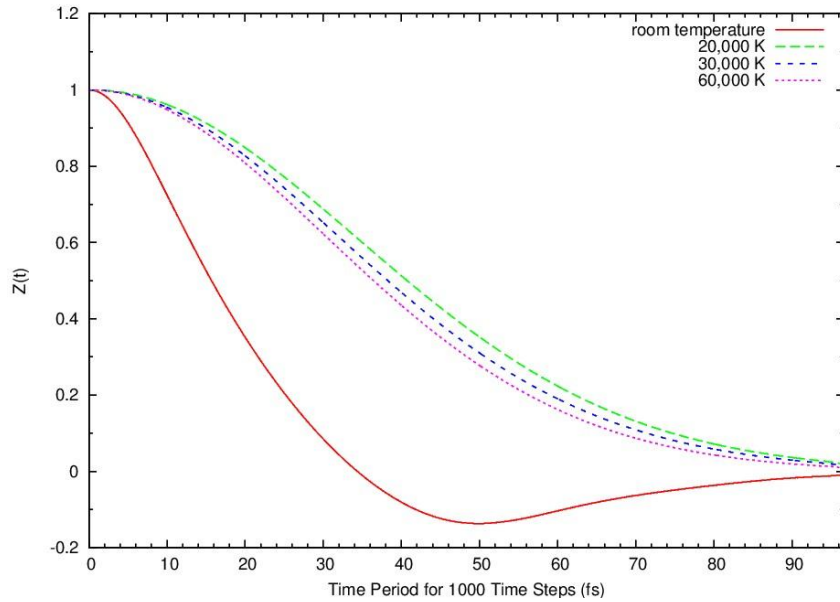


Fig. 24 VAFs of cases calculated from 1,000 time steps simulation

As is seen in Fig. 24, the computed VAFs for the last three cases are always positive, which lead to the high values of the diffusion coefficient. However, the VAF at room temperature contains both the positive part and negative part. The results can be interpreted in terms of the thermophysical interaction of atoms. Firstly, let us consider a single atom at time zero that has a specific velocity v . By assuming the atoms in the system do not interact with each other, according to the Newton's Second Law, the atom will retain the initial velocity all the time; the VAF profile will be a horizontal line with the evolution of time. If the forces are small but not negligible, then the magnitude of VAF will change gradually under the influence of the weak forces. Observing the green, blue and purple lines of the 20,000 K, 30,000 K and 60,000 K cases, one can see that the VAFs render simple decays, which demonstrates the presence of weak force slowly destroy the velocity correlations. For the solid germanium at room temperature, the atoms are compacted closely to each other. They will search the position at which there is a balance between the attractive and repulsive forces and the energies of the atoms can be regarded stable for such system. The motion of atoms is like dots connected by springs with back and forth oscillations, so the regular position cannot be broken down and disordered. Hence, the calculated VAF show strong oscillations from positive to negative values with periodicity. The red plot in Fig. 24 shows a damped harmonic motion, which verifies that the germanium at room temperature is a usual solid without excited electrons. But for the cases of solid and liquid germanium after femtosecond laser irradiation, they show the resemble shapes as the gas germanium. It is contradictory to the definition of phase based on the temperature, but such contradictories prove the validity of the discrepancies of germanium between $T_{e&l} = 400$ K and $T_l = 400$ K. It is speculated that

such solid and liquid germanium states as meta-states that differentiate from the usual solid and liquid in nature. In addition, we can find the curve of the 60,000 K is the steepest among the three. The most damped curve can be considered there are less collisions between two atoms and then diffuse away, which reflects the chemically covalence bond break due the exited electrons.

5.2.6 Vibrational Density of States Analysis

The vibrational density of states (VDOS) can be used to characterize the number of states per interval of energy at each energy level. We calculated the VDOS by performing Fourier transform of the VAF over all atoms. The normalized VDOS of N atoms system is given by

$$g(\nu) = \int_{-\infty}^{+\infty} \frac{\sum_{i=1}^N (\mathbf{V}_i(t) \cdot \mathbf{V}_i(0))}{\sum_{i=1}^N (\mathbf{V}_i(0) \cdot \mathbf{V}_i(0))} e^{2\pi i \nu t} dt \quad (52)$$

Thermal properties, such as the heat capacity and thermal conductivity as well as some other material properties are strongly impacted by the vibrational density of states (VDOS). Hence, to get a profound grasp of the laws governing the vibrational properties of femtosecond laser irradiated germanium is of high technological and fundamental interest. Figure 25 indicates there are high diffusive modes in the low frequency regions. But for the case of germanium with $T_{e\&l} = 300$ K at room temperature, the peak evidently distinguishes from the other three. Therefore, we can conclude that the VDOS of the cases have changed due to the phase transitions induced by the incident femtosecond laser.

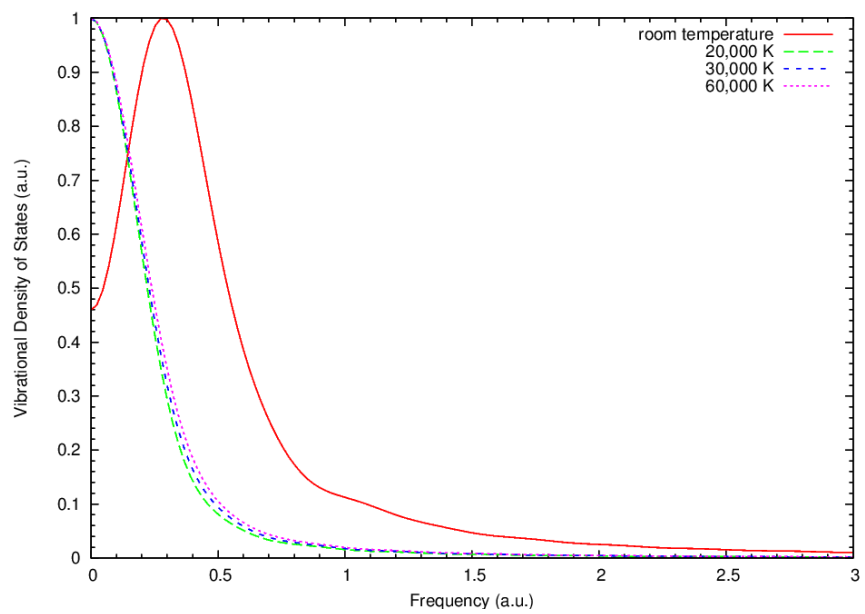


Fig. 25 VDOS of cases sample from 1,000 time steps simulation

Chapter 6 Summary and Conclusion

In summary, Ab initial molecular dynamics is used to simulated heat conduction, thermal radiation occurring in Si/Ge superlattices and the femtosecond laser nanolithography in the current thesis.

In chapter 3, the microstructure, translation dynamics and vibrational density of states of Si/Ge superlattices were studied with 64 atoms per specie. We adopt non-equilibrium MD simulations starting from the initial temperature of 800 K for silicon layer and 300 K for germanium layer. The entire simulation process was conducted by monitoring the temperatures of the two layers and the simulation was finally terminated when the system reached thermal equilibrium state. The computed RDFs and MSDs of each layer at different simulation stages demonstrate significant changes of the SLs structure and their relating characteristics. The structural changes are in consistent with the thermal motion of the atoms inside each layer. After obtaining the final equilibrium state between the layers, RDF curves of the two layers show almost the same probabilities, which reflect the same kinds of average structural responses at thermal equilibrium. The comparisons of lateral and longitudinal results of MSDs at the same simulation moments and evolutionary moments at different NVE simulation stages clearly show the MSD values variations as the heat conduction occurs. Because the interface transmission is crucial for building a bridge to calculate thermal energy transport of pure materials to compositing SLs, the computed VDOS from ab initial MD and the overlap areas of spectra indicate phonons locating in low frequency region indicate they are the main

contributors to enhance the thermal energy transport efficiency through the interface of the thin layers. In addition, interface roughness is a crucial factor that impedes the heat transfer. But for the model we established, the compositing materials are with similar crystal structures and are well matched in the initial simulation step. Since the Si/Ge superlattices are often applied as thermoelectric material, to get the low thermal conductivity is of great importance. Feasible approaches are modulating the vibrational frequencies to reduce the coherent heat transfer in the low frequencies regions and maximally increasing the phonon scattering at the interfaces and layer boundaries. We will introduce artificial patterns in the contacting surface of the layers to probe the heat transfer process and its efficiency in our further work.

In chapter 4, ab initio MD simulations of thermal conduction and radiation in combinations of silicon and germanium thin layers were carried out to investigate the energy transport process from non-equilibrium to equilibrium. Silicon-silicon-layer (400 K versus 100 K), germanium-germanium-layer (400 K versus 100 K), and silicon-germanium-layer (400 K versus 100 K and 100 K versus 400 K) combinations were simulated by gradually increasing interfacial distance between the neighboring layers. The effects of interfacial distance and material species were rendered via plotting of the temperature evolutions for the neighboring layers. From the heat conduction to thermal radiation process, equilibration time becomes longer, except for the combination of silicon (100 K) - germanium (400 K) - layer in the heat conduction case. With increasing the interfacial distance, the equilibration time becomes longer. Under the condition of the pure material combination (silicon–silicon-layer and germanium-germanium-layer), the thermal communication develops significantly faster than that of the hybrid materials

combinations (silicon-germanium-layer). The acoustic mismatch is the main factor that leads to difficult thermal communication for silicon-germanium-layer. In addition, mass differences and configurations of electrons surrounding nucleus are other factors. The distinct differences between silicon-germanium-layer under conditions of 400 K versus 100 K and 100 K versus 400 K indicate the interfacial thermal physical properties of nano-composite materials depend not only on the properties of their individual constituents but also their morphology and connection characteristics. Due to the different indexes of reflection of silicon and germanium, the evanescent waves generated by vibrations of charge dipoles are impeded under different critical angles and directly lead to longer equilibration time for high temperature germanium versus low temperature silicon combination.

In chapter 5, ab initio molecular dynamics study of the thermal and dynamic effect induced by femtosecond laser irradiation was performed. By employing the finite temperature density functional theory and incorporating with direct energy minimization, the accurate pseudopotential description of core electrons and the Nose Hoover dynamics temperature control of the electronic and ionic subsystem, our simulation successfully obtained the results of the germanium in three phases (solid, liquid and gas). Even though the simulation in the present work is simplified in some extent, we believe that it captures the essential melting and dynamic features induced by different thermal excitation of the electronic subsystems. The unmelt germanium show essentially liquid and gas characteristics that are different from the usual solid germanium without excited electrons around the nucleus. The nanostructures and maximum value of the atomic thermal motion depend on the excited levels of the thermalized electrons. The melting and

dynamic response of ionic system also depends on the incident laser intensity, which means the higher excited electronics subsystem, the rapider temperature response of the ionic subsystem. However, there are some thresholds for the energy of the electronic subsystem that limits the phase change from solid to liquid and liquid to gas phase. The melting and evaporation are determined by both the electronic and ionic sub systems.

To sum up, the thesis demonstrates the great potential of ab initio MD simulation of nanostructure materials. With the advantages over classical MD simulation and other numerical modeling methodologies, it is also possible to broaden the ab initio MD simulation to heat transfer problems involving the participation of electron interactions and transport. With the advantage of high accuracy of electron structure calculation, we believe that the ab initio molecular dynamics theory will serve as a novel approach to solve atomic-scale thermal transport problems in the future.

REFERENCES

- [1] Damaraju S., George V., Jahagirdar S., Khondker T., Milstrey R., Sarkar S., Siers S., Stoloro I., and Subbiah A., 2012, “A 22nm IA multi-CPU and GPU System-on-Chip,” Solid-State Circuits Conference Digest of Technical Papers (ISSCC), 2012 IEEE International, pp. 56–57.
- [2] Schaller R. R., 1997, “Moore’s law: past, present and future,” Spectrum, IEEE, **34**(6), pp. 52–59.
- [3] Esaki L., and Tsu R., 1970, “Superlattice and negative differential conductivity in semiconductors,” IBM Journal of Research and Development, **14**(1), pp. 61–65.
- [4] Cahill D. G., Ford W. K., Goodson K. E., Mahan G. D., Majumdar A., Maris H. J., Merlin R., and Phillpot S. R., 2003, “Nanoscale thermal transport,” Journal of Applied Physics, **93**(2), p. 793.
- [5] Shakouri A., 2006, “Nanoscale thermal transport and microrefrigerators on a chip,” Proceedings of the IEEE, **94**(8), pp. 1613–1638.
- [6] Volz S. G., and Chen G., 1999, “Molecular dynamics simulation of thermal conductivity of silicon nanowires,” Applied Physics Letters, **75**(14), p. 2056.
- [7] Spearing S. ., 2000, “Materials issues in microelectromechanical systems (MEMS),” Acta Materialia, **48**(1), pp. 179–196.

- [8] Chen G., 2006, “Nanoscale heat transfer and nanostructured thermoelectrics,” IEEE Transactions on Components and Packaging Technologies, **29**(2), pp. 238–246.
- [9] Cahill D. G., Ford W. K., Goodson K. E., Mahan G. D., Majumdar A., Maris H. J., Merlin R., and Phillpot S. R., 2003, “Nanoscale thermal transport,” Journal of Applied Physics, **93**(2), p. 793.
- [10] Chen G., 2000, “Phonon heat conduction in nanostructures,” International journal of thermal sciences, **0729**(57), pp. 471–480.
- [11] Chen G., 2000, “Particularities of Heat Conduction in Nanostructures,” Journal of Nanoparticle Research, **2**(2), pp. 199–204.
- [12] Lee S.-M., Cahill D. G., and Venkatasubramanian R., 1997, “Thermal conductivity of Si–Ge superlattices,” Applied Physics Letters, **70**(22), p. 2957.
- [13] Chen G., 1998, “Thermal conductivity and ballistic-phonon transport in the cross-plane direction of superlattices,” Physical Review B, **57**(23), pp. 14958–14973.
- [14] Kiselev A., Kim K., and Strosio M., 2000, “Thermal conductivity of Si/Ge superlattices: A realistic model with a diatomic unit cell,” Physical Review B, **62**(11), pp. 6896–6899.
- [15] Tamura S., Tanaka Y., and Maris H. J., 1999, “Phonon group velocity and thermal conduction in superlattices,” Physical Review B, **60**(4), pp. 2627–2630.

- [16] Zhang W., Mingo N., and Fisher T., 2007, "Simulation of phonon transport across a non-polar nanowire junction using an atomistic Green's function method," *Physical Review B*, **76**(19), p. 195429.
- [17] Mingo N., and Yang L., 2003, "Phonon transport in nanowires coated with an amorphous material: An atomistic Green's function approach," *Physical Review B*, **68**(24), p. 245406.
- [18] Chang C. W., Okawa D., Majumdar A., and Zettl A., 2006, "Solid-State Thermal Rectifier," *Science*, **414**(5802), pp. 1121–1124.
- [19] Yu J.-K., Mitrovic S., Tham D., Varghese J., and Heath J. R., 2010, "Reduction of thermal conductivity in phononic nanomesh structures.," *Nature Nanotechnology*, **5**(10), pp. 718–721.
- [20] Lim J., Hippalgaonkar K., Andrews S. C., Majumdar A., and Yang P., 2012, "Quantifying surface roughness effects on phonon transport in silicon nanowires.," *Nano Letters*, **12**(5), pp. 2475–2482.
- [21] De Wilde Y., Formanek F., Carminati R., Gralak B., Lemoine P.-A., Joulain K., Mulet J.-P., Chen Y., and Greffet J.-J., 2006, "Thermal radiation scanning tunnelling microscopy.," *Nature*, **444**(7120), pp. 740–3.
- [22] Howell J. R., Sigel R., and Menguc M. P., 2011, *Thermal Radiation Heat Transfer*, CRC Press.

- [23] Tzou D. Y., 1995, “A Unified Field Approach for Heat Conduction From Macro- to Micro-Scales,” *Journal of Heat Transfer*, **117**(1), pp. 8–16.
- [24] Narayanaswamy A., Shen S., and Chen G., 2008, “Near-field radiative heat transfer between a sphere and a substrate,” *Physical Review B*, **78**(11), pp. 1–4.
- [25] Hu L., Narayanaswamy A., Chen X., and Chen G., 2008, “Near-field thermal radiation between two closely spaced glass plates exceeding Planck’s blackbody radiation law,” *Applied Physics Letters*, **92**(13), p. 133106.
- [26] Volokitin A. I., and Persson B. N. J., 2001, “Radiative heat transfer between nanostructures,” *Physical Review B*, **63**(20), p. 205404.
- [27] Kittel A., Müller-Hirsch W., Parisi J., Biehs S.-A., Reddig D., and Holthaus M., 2005, “Near-Field Heat Transfer in a Scanning Thermal Microscope,” *Physical Review Letters*, **95**(22), pp. 1–4.
- [28] Koch J., Fadeeva E., Engelbrecht M., Ruffert C., Gatzert H. H., Ostendorf a., and Chichkov B. N., 2005, “Maskless nonlinear lithography with femtosecond laser pulses,” *Applied Physics A*, **82**(1), pp. 23–26.
- [29] Halbax M., Sarnet T., Delaporte P., Sentis M., Etienne H., Torregrosa F., Vervisch V., Perichaud I., and Martinuzzi S., 2008, “Micro and nano-structuration of silicon by femtosecond laser: Application to silicon photovoltaic cells fabrication,” *Thin Solid Films*, **516**(20), pp. 6791–6795.

- [30] König K., Raphael A. P., Lin L., Grice J. E., Soyer H. P., Breunig H. G., Roberts M. S., and Prow T. W., 2011, “Applications of multiphoton tomographs and femtosecond laser nanoprocessing microscopes in drug delivery research.,” *Advanced drug delivery reviews*, **63**(4-5), pp. 388–404.
- [31] Chau J. L. H., Chen C.-Y., Yang M.-C., Lin K.-L., Sato S., Nakamura T., Yang C.-C., and Cheng C.-W., 2011, “Femtosecond laser synthesis of bimetallic Pt–Au nanoparticles,” *Materials Letters*, **65**(4), pp. 804–807.
- [32] Della Valle G., Osellame R., and Laporta P., 2009, “Micromachining of photonic devices by femtosecond laser pulses,” *Journal of Optics A: Pure and Applied Optics*, **11**(1), p. 013001.
- [33] Bizi-Bandoki P., Benayoun S., Valette S., Beaugiraud B., and Audouard E., 2011, “Modifications of roughness and wettability properties of metals induced by femtosecond laser treatment,” *Applied Surface Science*, **257**(12), pp. 5213–5218.
- [34] Zhang Y., and Chen J. K., 2007, “Melting and resolidification of gold film irradiated by nano- to femtosecond lasers,” *Applied Physics A*, **88**(2), pp. 289–297.
- [35] Recoules V., Cl érouin J., Z érah G., Anglade P., and Mazevet S., 2006, “Effect of Intense Laser Irradiation on the Lattice Stability of Semiconductors and Metals,” *Physical Review Letters*, **96**(5), p. 055503.

- [36] Silvestrelli P. L. P., Parrinello M., Alavi A., and Frenkel D., 1996, “Ab initio Molecular Dynamics Simulation of Laser Melting of Silicon,” *Physical Review Letters*, **77**(15), pp. 3149–3152.
- [37] Shank C., Yen R., and Hirlimann C., 1983, “Femtosecond-time-resolved surface structural dynamics of optically excited silicon,” *Physical Review Letters*, **51**(10), pp. 900–902.
- [38] Rouse A., Rischel C., Fourmaux S., Uschmann I., Sebban S., Grillon G., Balcou P., Forster E., Geindre J. P. P., Audebert P., Gauthier J. C. C., Hulin D., and Förster E., 2001, “Non-thermal melting in semiconductors measured at femtosecond resolution,” *Nature*, **410**(6824), pp. 65–8.
- [39] Lindenberg A. M., Larsson J., Sokolowski-Tinten K., Gaffney K. J., Blome C., Synnergren O., Sheppard J., Coleman C., MacPhee a G., Weinstein D., Lowney D. P., Allison T. K., Matthews T., Falcone R. W., Cavalieri A. L., Fritz D. M., Lee S. H., Bucksbaum P. H., Reis D. A., Rudati J., Fuoss P. H., Kao C. C., Siddons D. P., Pahl R., Als-Nielsen J., Duesterer S., Ischebeck R., Schlarb H., Schulte-Schrepping H., Tschentscher T., Schneider J., Von der Linde D., Hignette O., Sette F., Chapman H. N., Lee R. W., Hansen T. N., Techert S., Wark J. S., Bergh M., Hultdt G., Van der Spoel D., Timneanu N., Hajdu J., Akre R. A., Bong E., Krejcik P., Arthur J., Brennan S., Luening K., and Hastings J. B., 2005, “Atomic-Scale Visualization of Inertial Dynamics,” *Science*, **308**(5720), pp. 392–395.

- [40] Alder B. J., and Wainwright T. E., 1957, "Phase Transition for a Hard Sphere System," *Journal of Chemical Physics*, **27**(5), pp. 1208–1209.
- [41] Alder B. J., and Wainwright T. E., 1959, "Studies in Molecular Dynamics. I. General Method," *Journal of Chemical Physics*, **31**(2), pp. 459–466.
- [42] Tuckerman M. E. M., and Martyna G. J. G., 1999, "Understanding Modern Molecular Dynamics: Techniques and Applications," *Journal of Physical Chemistry B*, **104**(2), pp. 159–178.
- [43] Sutmann G., 2002, "Classical Molecular Dynamics," *Quantum Simulations of Complex Many-Body Systems: From Theory to Algorithms*, **10**, pp. 211–254.
- [44] Chalopin Y., Esfarjani K., Henry a., Volz S., and Chen G., 2012, "Thermal interface conductance in Si/Ge superlattices by equilibrium molecular dynamics," *Physical Review B*, **85**(19), pp. 1–7.
- [45] Search H., Journals C., Contact A., Iopscience M., and Address I. P., 2003, "Lattice thermal conductivity in superlattices: molecular dynamics calculations with a heat reservoir," **8679**.
- [46] Termentzidis K., Chantrenne P., and Koblinski P., 2009, "Nonequilibrium molecular dynamics simulation of the in-plane thermal conductivity of superlattices with rough interfaces," *Physical Review B*, **79**(21), p. 214307.

- [47] Marx D., and Hutter J., 2000, “Ab initio molecular dynamics: theory and implementation,” *Modern Methods and Algorithms of Quantum Chemistry*, **1**, pp. 301–449.
- [48] Payne M. C., Teter M. P., Allan D. C., Arias T. A., Joannopoulos J. D., Payne C., and York N., 1992, “Iterative minimization techniques for ab initio total-energy calculations: molecular dynamics and conjugate gradients,” *Reviews of Modern Physics*, **64**(4), pp. 1045–1097.
- [49] Luo T., and Lloyd J. R., 2008, “Ab Initio Molecular Dynamics Study of Nanoscale Thermal Energy Transport,” *Journal of Heat Transfer*, **130**(12), p. 122403.
- [50] De Koker N., 2009, “Thermal Conductivity of MgO Periclase from Equilibrium First Principles Molecular Dynamics,” *Physical Review Letters*, **103**(12), pp. 1–4.
- [51] Crisp D., Pathare a., and Ewell R. C., 2004, “The performance of gallium arsenide/germanium solar cells at the Martian surface,” *Acta Astronautica*, **54**(2), pp. 83–101.
- [52] Washio K., 2003, “SiGe HBT and BiCMOS technologies for optical transmission and wireless communication systems,” *Electron Devices, IEEE Transactions on*, **50**(3), pp. 656–668.
- [53] Silvestrelli P. L., and Parrinello M., 1998, “Ab initio Molecular Dynamics Simulation of Laser Melting of Graphite,” *Journal of Applied Physics*, **83**(5), p. 2478.

- [54] Alavi A., Kohanoff J., Parrinello M., and Frenkel D., 1994, “Ab Initio Molecular Dynamics with Excited Electrons,” *Physical Review Letters*, **73**(19), pp. 2599–2602.
- [55] Kohn W., Becke A. D., and Parr R. G., 1996, “Density Functional Theory of Electronic Structure,” *The Journal of Physical Chemistry*, **100**(31), pp. 12974–12980.
- [56] Städele M., Moukara M., Majewski J. A., Vogl P., and Görling A., 1999, “Exact exchange Kohn-Sham formalism applied to semiconductors,” *Physical Review B*, **59**(15), pp. 10031–10043.
- [57] Car R., and Parrinello M., 1985, “Unified Approach for Molecular Dynamics and Density-Functional Theory,” *Physical Review Letters*, **55**(22), pp. 2471–2474.
- [58] Car R., Štich I., and Parrinello M., 1991, “Structural, bonding, dynamical, and electronic properties of liquid silicon: An ab initio molecular-dynamics study,” *Physical Review B*, **44**(9), pp. 4262–4274.
- [59] Pastore G., Smargiassi E., Smargiassi E., and Buda F., 1991, “Theory of ab initio molecular-dynamics calculations,” *Physical Review A*, **44**(10), pp. 6334–6347.
- [60] Car R., and Parrinello M., 1985, “Unified Approach for Molecular Dynamics and Density-Functional Theory,” *Physical Review Letters*, **55**(22), pp. 2471–2474.

- [61] Stoks V. G. J., Klomp R. A. M., Terheggen C. P. F., and De Swart J. J., 1994, “Construction of high-quality NN potential models,” *Physical Review C*, **49**(6), pp. 2950–2962.
- [62] Pashov A., and Jastrz W., 2000, “Construction of potential curves for diatomic molecular states by the IPA method,” **128**, pp. 622–634.
- [63] Mermin N. D., 1965, “Thermal Properties of the Inhomogeneous Electron Gas,” *Physical Review*, **137**(5A), pp. A1441–A1443.
- [64] Parlett B., and Scott D., 1979, “The Lanczos algorithm with selective orthogonalization,” *Mathematics of computation*, **33**(145), pp. 217–238.
- [65] “CPMD,” <http://www.cpmc.org/>, Copyright IBM Corp 1990-2008, Copyright MPI fur Festkorperforschung Stuttgart 1997-2001.
- [66] Humphrey W., Dalke A., and Schulten K., 1996, “VMD - Visual Molecular Dynamics.pdf,” *J. Molec. Graphics*, **14**(1), pp. 33–38.
- [67] Stukel D. J., and Euwema R. N., 1970, “Self-Consistent Orthogonalized-Plane-Wave Energy-Band Study of Silicon,” *Physical Review B*, **1**(4), pp. 1635–1643.
- [68] Kim D. H., Hwang E., Hong S., and Kim S., 2006, “Atomic and electronic structure of acetic acid on Ge(1 0 0),” *Surface Science*, **600**(18), pp. 3629–3632.

- [69] Lee C., Hill C., Carolina N., Yang W., and Parr R. G., 1988, “Development of the Colle-Salvetti correlation-energy formula into a functional of the electron density,” *Physical Review B*, **37**(2), pp. 785–789.
- [70] Becke A. D., and Perdew J. P., 1988, “Density-functional exchange-energy approximation with correct asymptotic behavior,” *Physical Review A*, **38**(6), pp. 3098–3100.
- [71] Troullier N., and Martins J. J. L., 1991, “Efficient pseudopotentials for plane-wave calculations,” *Physical Review B*, **43**(3), pp. 1993–2006.
- [72] Nose S., 1999, “Constant-temperature molecular dynamics,” *Journal of Physics: Condensed Matter*, **115**(2), pp. SA115–SA119.
- [73] Le Roux S., and Petkov V., 2010, “ISAACS – interactive structure analysis of amorphous and crystalline systems,” *Journal of Applied Crystallography*, **43**(1), pp. 181–185.
- [74] Luo T., and Lloyd J. R., 2008, “Ab Initio Molecular Dynamics Study of Nanoscale Thermal Energy Transport,” *Journal of Heat Transfer*, **130**(12), p. 122403.
- [75] Ballone P., Andreoni W., Car R., and Parrinello M., 1988, “Equilibrium Structures and Finite Temperature Properties of Silicon Microclusters from ab initio Molecular-Dynamics Calculations,” *Physical Review Letters*, **60**(4), pp. 271–274.

- [76] Germany W., Soukoulis C. M., Shanks H. R., Kamitakahara W. A., Buchenau U., and Grest G. S., 1987, “Vibrational spectrum of amorphous silicon: Experiment and computer simulation,” *Physical Review B*, **36**(12), pp. 6539–6542.
- [77] Luckyanova M. N., Garg J., Esfarjani K., Jandl a., Bulsara M. T., Schmidt a. J., Minnich a. J., Chen S., Dresselhaus M. S., Ren Z., Fitzgerald E. a., and Chen G., 2012, “Coherent Phonon Heat Conduction in Superlattices,” *Science*, **338**(6109), pp. 936–939.
- [78] Troullier N., and Martins J., 1991, “Efficient pseudopotentials for plane-wave calculations. II. Operators for fast iterative diagonalization,” *Physical Review B*, **43**(11), pp. 8861–8869.
- [79] Gonze X., Stumpf R., and Scheffler M., 1991, “Analysis of separable potentials,” *Physical Review B*, **44**(16), pp. 8503–8513.
- [80] Icenogle H. W., Platt B. C., and Wolfe W. L., 1976, “Refractive indexes and temperature coefficients of germanium and silicon.,” *Applied optics*, **15**(10), pp. 2348–51.
- [81] Ahn D., Kimerling L. C., and Michel J., 2011, “Efficient evanescent wave coupling conditions for waveguide-integrated thin-film Si/Ge photodetectors on silicon-on-insulator/germanium-on-insulator substrates,” *Journal of Applied Physics*, **110**(8), p. 083115.

- [82] Goedecker S., Teter M., and Hutter J., 1996, "Separable dual-space Gaussian pseudopotentials," *Physical Review B*, **54**(3), pp. 1703–1710.
- [83] Kresse G., and Hafner J., 1994, "Norm-conserving and ultrasoft pseudopotentials for first-row and transition elements," *Journal of Physics: Condensed Matter*, **6**(40), p. 8245.
- [84] Sen S., and Dickinson J., 2003, "Ab initio molecular dynamics simulation of femtosecond laser-induced structural modification in vitreous silica," *Physical Review B*, **68**(21), p. 214204.
- [85] Sokolowski-Tinten K., and Bialkowski J., 1998, "Thermal and nonthermal melting of gallium arsenide after femtosecond laser excitation," *Physical Review B*, **58**(18), pp. 11805–11808.
- [86] Oxtoby D. W., 1990, "New perspectives on freezing and melting," *Nature*, **347**(25), pp. 725–730.
- [87] Bonse J., Baudach S., Krüger J., Kautek W., and Lenzner M., 2002, "Femtosecond laser ablation of silicon-modification thresholds and morphology," *Applied Physics A*, **25**(74), pp. 19–25.
- [88] Silvestrelli P., Alavi A., Parrinello M., and Frenkel D., 1997, "Structural, dynamical, electronic, and bonding properties of laser-heated silicon: An ab initio molecular-dynamics study," *Physical Review B*, **56**(7), pp. 3806–3812.